Spatiotemporal lineage tracing reveals the dynamic spatial architecture of tumor growth and metastasis

Matthew G. Jones[1,18], Dawei Sun[2,3,18], Kyung Hoi (Joseph) Min[4,5,6], William N. Colgan[4,5], Luyi Tian[2], Jackson A. Weir[2,7], Victor Z. Chen[8,9], Luke W. Koblan[4,5], Kathryn E. Yost[4,5], Nicolas Mathey-Andrews[5,10,11], Andrew J.C. Russell[2,3], Robert R. Stickels[2], Karol S. Balderrama[2], William M. Rideout III[10], Howard Y. Chang[1,13,14], Tyler Jacks[5,10], Fei Chen[2,3,#], Jonathan S. Weissman[4,5,10,15,#], Nir Yosef[16,#], Dian Yang[8,9,17,19,#]

[1] Center for Personal Dynamic Regulomes, Stanford University, Stanford, CA, USA.
[2] Broad Institute of MIT and Harvard, Cambridge, MA, USA
[3] Department of Stem Cell and Regenerative Biology, Harvard University, Cambridge, MA, USA
[4] Whitehead Institute for Biomedical Research, Cambridge, MA, USA
[5] Department of Biology, Massachusetts Institute of Technology, Cambridge, MA, USA
[6] Department of Electrical Engineering and Computer Science, Massachusetts Institute of Technology, Cambridge, MA, USA
[7] Biological and Biomedical Sciences Program, Harvard University, Cambridge, MA, USA
[8] Department of Molecular Pharmacology and Therapeutics, Columbia University, New York City, NY, USA
[9] Department of Systems Biology, Columbia University, New York City, NY, USA
[10] David H. Koch Institute for Integrative Cancer Research, Massachusetts Institute of Technology, Cambridge, MA, USA
[11] Harvard Medical School, Boston, MA, USA
[13] Department of Genetics, Stanford University, Stanford, CA, USA
[14] Howard Hughes Medical Institute, Stanford University School of Medicine, Stanford, CA, USA
[15] Howard Hughes Medical Institute, Massachusetts Institute of Technology, Cambridge, MA, USA
[16] Department of Systems Immunology, Weizmann Institute of Science, 234 Herzl Street, Rehovot 7610001, Israel
[17] Herbert Irving Comprehensive Cancer Center, Columbia University, New York City, NY, USA
[18] These authors contributed equally.
[19] Lead Contact

[#] Co-correspondence: : chenf@broadinstitute.org (F.C.), weissman@wi.mit.edu (J.S.W.), niryosef@berkeley.edu (N.Y.), dy2491@cumc.columbia.edu (D.Y.)

ABSTRACT

Tumor progression is driven by dynamic interactions between cancer cells and their surrounding microenvironment. Investigating the spatiotemporal evolution of tumors can provide crucial insights into how intrinsic changes within cancer cells and extrinsic alterations in the microenvironment cooperate to drive different stages of tumor progression. Here, we integrate high-resolution spatial transcriptomics and evolving lineage tracing technologies to elucidate how tumor expansion, plasticity, and metastasis co-evolve with microenvironmental remodeling in a *Kras;p53*-driven mouse model of lung adenocarcinoma. We find that rapid tumor expansion contributes to a hypoxic, immunosuppressive, and fibrotic microenvironment that is associated with the emergence of pro-metastatic cancer cell states. Furthermore, metastases arise from spatially-confined subclones of primary tumors and remodel the distant metastatic niche into a fibrotic, collagen-rich microenvironment. Together, we present a comprehensive dataset integrating spatial assays and lineage tracing to elucidate how sequential changes in cancer cell state and microenvironmental structures cooperate to promote tumor progression.

INTRODUCTION

Tumor progression is driven by the dynamic interactions between cancer cells[1,2] and the their surrounding microenvironment[3,4]. In this process, as cancer cells accumulate genetic and epigenetic alterations, the microenvironment exerts selective pressures through factors such as spatial constraints[5,6], signaling molecules[7], nutrient and oxygen availability[8,9], and immune infiltration[3,10] among other phenomena. In turn, tumor growth remodels the surrounding microenvironment, for example, by restructuring the extracellular matrix and altering the composition and state of infiltrating stromal cells[11]. Systematically characterizing the cell intrinsic and extrinsic effects that drive tumor subclonal selection, cellular plasticity, and metastasis will not only provide insights into the principles of tumor evolution but also carry clinical implications. To accomplish this, one must study a tumor's evolutionary dynamics alongside its microenvironmental composition in the native spatial context.

Integrating tumor phylogenetic analysis, the study of lineage relationships of cancer cells within a tumor[12–17], with spatial information provides a comprehensive framework for understanding the interplay between tumor microenvironment and progression. Specifically, spatially resolved phylogenetic studies enable one to approach key questions in cancer evolution such as, what are the major spatial communities that exist in tumors, and how do these relate to tumor stage? From which spatial niches do subclonal expansions arise during tumor progression, and how does this relate to tumor plasticity and the capacity to seed metastases? And, how does

69 the spatial growth pattern of tumor progression shape the surrounding microenvironment? Early
70 studies reconstructing tumor phylogenies from multi-region sampling of patient tumors uncovered
71 the spatial heterogeneity of genetic changes within tumors and have demonstrated the dynamics
72 of tumor growth and spatially-constrained origins of metastatic dissemination[18–24]. More recently,
73 spatial genomics approaches have further elucidated how the spatial distribution of genome
74 alterations leads to clonal outgrowth, dispersion of subclones with distinct driver mutations,
75 interactions with the immune system, and metastasis[25–29]. While these studies have greatly
76 enhanced our understanding of how tumors grow in space and time, they can be limited in their
77 ability to either resolve high-resolution spatial organization, infer deeper phylogenetic
78 relationships of cancer cells, or simultaneously measure the microenvironmental composition and
79 gene expression.

80 The development of molecular recording technologies that install evolving lineage-tracing
81 barcodes[30–40] and associated computational tools[41–46] enable the reconstruction of high-resolution
82 phylogenies for studying tumor evolution[13]. Typically, these lineage-tracing technologies employ
83 genome-editing tools, such as CRISPR/Cas9, to introduce heritable and irreversible mutations
84 progressively at defined genomic loci, which can be transcribed and thus profiled with single-cell
85 RNA-seq. In cancer, initial studies applied this technology to track the metastatic dynamics of
86 cancer cell lines transplanted into mice[47–49]. Previously, we described a lineage-tracing enabled
87 genetically-engineered mouse model of *Kras*$^{LSL\text{-}G12D/+}$;*Trp53*$^{fl/fl}$-driven lung adenocarcinoma (KP-
88 Tracer) to continuously track tumor evolution from nascent transformation of single cells to
89 aggressive metastasis[50]. In this system, intratracheal delivery of *Cre* recombinase using viral
90 vectors simultaneously induces Cas9-based lineage tracing and tumor initiation. This model
91 recapitulates the major steps of the evolution of human lung adenocarcinoma, both molecularly
92 and histopathologically[51–55]. Using this system, we recently identified subclonal expansions,
93 quantified tumor plasticity, traced metastatic origins and routes, and disentangled the effect of
94 genetic drivers on tumor evolution. However, as our previous applications have relied on studying
95 dissociated single cells, it has remained unclear how key tumor evolutionary properties are
96 associated with microenvironmental changes.

97 Here, we present an integrated lineage and spatial platform for tracking tumor evolution *in*
98 *situ* by applying high-resolution spatial transcriptomics to our lineage tracing-enabled KP-Tracer
99 model. Using two complementary spatial transcriptomics assays – Slide-seq[56,57] with spot-based
100 coverage at 10μm near-cell resolution of large tissue fields-of-view, and Slide-tags[58] with higher
101 molecular sensitivity and spatial profiling of individual nuclei – we produce a comprehensive
102 spatial transcriptomics dataset of *Kras;p53*-driven lung adenocarcinoma evolution. Integrating

these spatial transcriptomics data with inferred cancer cell lineages uncovered robust spatial communities associated with tumor progression, including the formation of a hypoxic tumor interior during rapid tumor subclonal expansion. Our analysis additionally reveals that this hypoxic environment is associated with pervasive tissue remodeling characterized by fibrosis, priming of immune cells, and the emergence of a pro-metastatic epithelial-to-mesenchymal transition (EMT). Together, this study provides a scalable platform for studying the relationship between tissue architecture and tumor progression, revealing key insights into the ecological and evolutionary dynamics underpinning tumor evolution at unprecedented resolution.

RESULTS

An integrated lineage and spatial platform for studying tumor evolution

To study tumor evolution while preserving the native spatial context of cancerous and stromal tissue, we integrated spatial transcriptomics methods with Cas9-based lineage-tracing technology in our previously described KP-Tracer model of lung adenocarcinoma[50]. This model is built upon the well-characterized model of *Kras;Trp53*-driven lung adenocarcinoma[51,52,54,55] and is equipped with a *Cre*-inducible Cas9-based evolving lineage tracer that is able to continuously record high-resolution cell lineages over months-long timescales[32,41]. Introduction of *Cre* into individual lung cells in the adult animal both induces the oncogene mutations (i.e., expression of $Kras^{G12D}$ and homozygous loss of *p53*) and initiates Cas9 expression. Cas9 then introduces irreversible and heritable insertions and deletions ("indels") at defined genomic "target sites", each discernable by a random 14bp integration barcode ("intBC") and expressed as a polyadenylated transcript. As most sequencing-based spatial transcriptomics assays capture polyadenylated transcripts from tissue sections[56–60], applying these assays to the KP-Tracer model yields simultaneous measurement of spatially-resolved cell transcriptional states and lineage relationships.

We initiated lung tumors and lineage-tracing in alveolar type II (AT2) cells (a major cell of origin for lung adenocarcinoma) by intratracheally delivering adenovirus expressing *Cre* recombinase under the control of an AT2 cell-specific, surfactant Protein C (SPC) gene promoter[61]. Twelve to sixteen weeks post tumor initiation, tumor bearing lungs were harvested for cryopreservation, and then sectioned and applied to spatial transcriptomics arrays (**Figure 1A; Methods**). To comprehensively profile the spatiotemporal evolution of tumor progression, we utilized two complementary spatial transcriptomics technologies: Slide-seq[56,57] that captures transcriptomic states of "spots" at near-cellular 10μm resolution in continuous, large fields-of-view (up to 1cm x 1cm); and Slide-tags[58] that sparsely samples individual nuclei for transcriptomic

profiling and provides accurate spatial localization for a subset of these nuclei (typically ~50-70%). Together, this combination marries the scale of Slide-seq and true single-nucleus resolution of Slide-tags to jointly measure spatially resolved cell lineage and unbiased transcriptomic states in the native tumor microenvironment.

With these two technologies, we comprehensively profiled tumor-bearing lungs across various stages of progression with 44 Slide-seq arrays and 5 Slide-tags arrays (**Figure S1A-C**; **Methods**; **Supplementary Table 1**). The resulting datasets provided spatial profiling of distinct domains in tumor-bearing tissues characterized by the expression of canonical marker genes and corroborated by paired H&E: for example, in the tumor-bearing lung we found that *Cxcl15* and *Scgb1a1* marked epithelial-like domains, representing alveolar and club cells, respectively. Moreover, histologically aggressive regions were marked by *Vim* (characteristic of mesenchymal-like cancer cells) and *Arg1* (characteristic of immunosuppressive myeloid cells[62]) **(Figure 1B**). Altogether, these datasets provide high-resolution views into the microenvironmental context and organization of tumors.

Computational tools enable the inference of spatially resolved cancer cell phylogenies

As the KP-Tracer system expresses lineage tracing target-sites as poly-adenylated transcripts, we next turned to evaluating the recovery of these target sites from the complementary spatial transcriptomics platforms. Reassuringly, we detected target-site transcripts robustly across tens-of-thousands of spots or nuclei in these spatial datasets, with Slide-tags data having more consistent detection of target-sites as expected (**Figure 1C; Figure S1D-E**).

While Slide-tags provided true single-cell measurements and thus were amenable to previously-described lineage reconstruction approaches[41,44], there were two predominant analytical challenges in reconstructing tumor phylogenies of tens-of-thousands of spots observed in Slide-seq data. First, Slide-seq captures RNA molecules with near-cellular resolution, meaning that each spot may contain RNAs originating from multiple cells[57]; similarly, cells with distinct lineage states can be captured in a single spot, which we term “conflicting states”. As prior phylogenetic reconstruction algorithms for Cas9-lineage tracing data presume mapping of cells to single states, we first implemented new Cassiopeia-Greedy[41] and Neighbor-Joining[63] variants that could use many conflicting states during reconstruction (**Methods**). We also tested the effects of three strategies for preprocessing conflicting states via simulation: (1) a strategy that used all conflicting states observed in a spot along with the abundance of each state in that spot (“all states”); (2) all conflicting states observed in a spot, but without considering their abundance

171 (“collapse duplicates”); or (3) a strategy that used only the most abundant state (“most abundant”).
172 We found that the second strategy (“collapse duplicates”) performed most robustly (**Figure S1F**;
173 **Methods**).
174 A second challenge is that Slide-seq assays (and to a lesser extent Slide-tags) have an
175 increased missing data rate relative to droplet-based single-cell assays[64]. As expected, we
176 observed overall lower target-site transcript capture (and thus higher missing data) in Slide-seq
177 datasets (**Figure S1D,G**). We hypothesized that spatial relationships could be used to overcome
178 this sparsity, which was supported by our observations that indel states were coherent within
179 small spatial neighborhoods (**Figure S1H-I**). We therefore developed an inferential approach that
180 predicted missing lineage-tracing states from spatial neighbors (within 30μm of a target node)
181 with sufficient recovery (at least 3 UMI supporting a target site intBC-indel combination; **Figure**
182 **1D**). We first tested the feasibility of this approach using simulations of lineage tracing data on
183 spatial arrays using Cassiopeia (**Methods)**. We found that missing lineage-tracing barcodes could
184 consistently be recovered at high accuracy (**Figure S1J**), and that spatial imputation followed by
185 tree inference by a hybrid algorithm consisting of the Cassiopeia-Greedy and Neighbor-Joining
186 algorithms resulted in the best reconstructions, especially in high-dropout regimes (**Figure S1K-**
187 **L**; **Methods**). Next, we tested our ability to recover held-out target site data from real Slide-seq
188 data and similarly found that missing data could be robustly recovered by spatial predictions,
189 resulting in a median accuracy of 90% on imputing held-out data across all experiments, matching
190 our simulation results (random predictions had a median accuracy of 67% and yielded 29% fewer
191 imputations; **Figure S1M**). As expected, more frequent alleles had higher imputation accuracy
192 (**Figure S1N**; **Methods**). Over multiple iterations of this imputation algorithm, we found that we
193 could recover up to 58% of missing data (4-58%, on average 31% across datasets), resulting in
194 comparable missing data rates to previous reports using single-cell approaches that have enabled
195 robust tree reconstruction and biological insights (**Figure 1D, Figure S1O**). Though we only retain
196 high-confidence imputations, and our benchmarks point to the promise of this spatial imputation
197 in this context, there are notable caveats especially in the case of cell migration (see **Limitations**
198 **of this Study**). Combining Slide-seq data and validation from orthogonal trees provided by Slide-
199 tags establish a foundation for studying the spatial lineages of cancer cells.
200 Together, these computational improvements enabled us to build lineages of cancer cells
201 in the native context of a tumor’s microenvironment at unprecedented resolution (**Figure 1E**). Our
202 lineages revealed phylogenetic relationships in structured spatial environments and enabled us
203 to explore the spatial localization of increasingly related subclones within the same tumor (**Figure**

204 **1E**, **Figure S1P)**. With these data and approaches, we turned to investigating the relationship
205 between changes to the microenvironmental architecture and tumor progression.
206
207 **Spatial transcriptomics reveal the ecosystems of lung adenocarcinoma**
208 While recent efforts have studied the composition of tumors in this model using single-cell
209 approaches[50,54,55], it has remained challenging to profile the spatial organization of these cell
210 types. To address this, we leveraged the complementary insights gained from the high sensitivity,
211 true single-nucleus measurements of Slide-tags and the broad field-of-view of Slide-seq to
212 perform a systematic analysis of tumor spatial organization across stages of progression
213 observed in our 49 spatial transcriptomics arrays representing more than 100 tumors.
214 Focusing first on the true single nuclei profiled with Slide-tags, we performed fine-grained
215 annotation of clusters consisting of normal epithelial, stromal, immune, and tumor cells
216 (determined by canonical marker genes and the presence of active lineage-tracing edits) (**Figure**
217 **2A-B**; **Figure S2A**; **Methods**). In addition to annotating previously described tumor and normal
218 epithelial cells in this model[50,55], we identified a previously undescribed tumor cell state
219 characterized by the expression of neuronal genes such *Piezo2* and *Robo1,* the endothelial
220 marker *Pecam1,* maintenance of the lung-lineage transcription factor *Nkx2-1*, and absence of *Vim*
221 (**Figure S2B-C**). Although this cell type expressed active lineage tracing marks in our system, it
222 is likely that this cell type was excluded in previous studies[50,55,65] by purifying cancer cells against
223 CD31 expression (also known as *Pecam1*, expressed in this population) prior to transcriptomic
224 profiling; this highlights the advantage of spatial transcriptomics in profiling all cells and
225 communities, eliminating potential biases arising from tissue dissociation and preparation. In the
226 immune and stromal compartment, we observed large macrophage, fibroblast, and endothelial
227 populations with lower representation of B cells and dendritic cells (**Figure 2A**; **Figure S2A**).
228 Among macrophages, we detected *SiglecF*+ tissue-resident alveolar macrophages and three
229 distinct tumor-associated macrophage (TAM) populations: *Vegfa*+ TAMs, immunosuppressive
230 *Arg1*+ TAMs, and proangiogenic *Pecam1*+ TAMs (**Figure 2A)**. We additionally detected a diverse
231 set of cancer-associated fibroblasts (CAFs): a mesothelial-like *Wt1*+ population, an inflammatory-
232 like CAF ("iCAF") population expressing the complement gene *C7* and *Abca8a*, and a
233 myofibroblast-like CAF ("myCAF") population expressing *Postn* (**Figure 2A, Figure S2A**).
234 To explore the spatial localization of these diverse cell states, we assigned spatial
235 locations to Slide-tags nuclei and spatially projected cell identities. Consistent with previous
236 characterizations of Slide-tags spatial mapping rates[14], we found that approximately 50% of nuclei
237 could be confidently assigned to a spatial location (**Figure S2D**). Across the five Slide-tags arrays,

238 we observed a distinct pattern where less aggressive, “early-stage” tumor cell states (i.e., AT2-
239 and AT1-like cancer cells, indicated by expression of active lineage marks and distinct gene
240 expression from normal AT2 and AT1 cells) co-localized on the periphery of tumor sections
241 consisting of more aggressive “late stage” tumor cells (**Figure 2C, Figure S2E**). Similar to
242 previous work in this model[66], we also found that distinct immune and stromal cell types exhibited
243 differential infiltration – for example, Alveolar Macrophages and iCAFs were typically found
244 outside tumors, whereas *Arg1*+ TAMs and myCAFs were more likely to be found within tumors
245 (**Figure 2C, Figure S2E)**.

246 The spatially-localized transcriptional signatures observed with Slide-tags motivated us to
247 pair this approach with Slide-seq assays to survey the spatial gene expression communities
248 across large tissue areas in tumors. We thus turned to the 44 tissue sections assayed with Slide-
249 seq that collectively represent more than 100 tumors at various tumor stages. To identify modules
250 of genes that were recurrently spatially co-expressed across multiple samples, we employed the
251 Hotspot[33] algorithm (**Methods**). Our analysis revealed 11 recurrent spatial gene modules,
252 hereafter referred to as “communities” (**Figure 2D-E**), that we annotated by inspecting the genes
253 contained within communities and evaluating the expression level of community genes (captured
254 in a “community score”) in cell types identified by Slide-tags data (**Figure S2F-G)**.

255 The genes contained within these transcriptional communities represent a variety of co-
256 localized gene expression states: for example, an early-stage alveolar-like community contained
257 genes marking epithelial cells such as *Sftpc* and *Cxcl15* (“C1: Alveolar”), a hypoxic community
258 contained canonical marker genes of hypoxia such as *Slc2a1* (also known as *Glut1*) (“C10:
259 Hypoxia”), and an epithelial-to-mesenchymal (EMT) community contained genes such as
260 *Vim*, up-regulation of *Myc* signaling, and metastasis-related genes such as *Hmga2* (“C3: EMT”;
261 **Figure 2D-E, Figure S2G**). In addition to fibroblast (C5), B cell (C6), and endothelial (C7)
262 communities, we identified two distinct immunoregulatory-related communities. The first
263 community contained genes associated with scavenger-like macrophages like *Marco* and *Mrc1*
264 (“C8: Scavenger Mac”); a second community contained genes characteristic of inflammation such
265 as *B2m*, *Stat1*, and *Ifit1* (“C9: Inflammatory”). As these communities describe genes co-expressed
266 in spatial proximity, they provide insights into possible intercellular interactions. For example, the
267 EMT and hypoxic communities (C3 and C10) contained genes associated with macrophage
268 recruitment (e.g. *Csf1)* and polarization to immunosuppressive states that have been previously
269 reported to promote aggressive cancer phenotypes (e.g., *Arg1*[62] and *Spp1*[67]*)*, while the
270 Inflammatory community (C9) contained *Cxcl9* that has been previously reported in anti-tumor
271 macrophage polarization[67] (**Figure S2G**).

To inspect the distribution of these communities across large tissue sections profiled with Slide-seq, we quantified community scores for each spot and assigned spots to the community with the highest score (**Figure 2E-F, Figure S2H-I**). In comparing histology from an adjacent layer to the community scores, we found co-localization between areas indicating high tumor grade (as indicated by histology) and high scores for EMT, hypoxic, and fibrotic communities (C3, C10, C5; **Figure S2H**). We next asked how the distribution of community assignments varied over tumor stages using a gene set signature we previously identified to robustly associate with tumor progression (termed a "fitness signature")[50] (**Figure 2F; Figure S2I**; **Methods**). Specifically, this fitness signature contains genes that are associated with subclonal expansions in this model, and their collective activity (i.e., "score") reflects tumor progression towards an aggressive, pro-metastatic state. Consistent with the definition of this signature, after ranking tumors by their fitness signature score and inspecting the proportion of community assignments, we observed that early-stage tumors were dominated by epithelial, endothelial, and inflammatory communities (C1, C7, and C8, respectively) but that late-stage tumors had larger fractions of EMT, hypoxic, and fibroblast communities (C3, C10, and C5, respectively; **Figure 2F, Figure S2I**). Moreover, we found that overall abundances of EMT, hypoxic, and fibroblast community assignments (C3, C10, and C5, respectively) were correlated across all tumors; conversely, they were anticorrelated with the abundances of alveolar and inflammatory communities (C1 and C8, respectively) (**Figure 2G**).

Together, these analyses unite the unique advantages of Slide-tags and Slide-seq assays to provide a consensus set of spatial communities that highlight differential immune and stromal activation and localization patterns across tumor progression in KP tumors. These observations motivated us to next integrate our phylogenies to understand how the spatiotemporal dynamics of these communities are associated with tumor plasticity and subclonal expansion.

Rapid tumor subclonal expansion contributes to a hypoxic niche with decreased cancer cell plasticity

Integrating cell state information with high-resolution phylogenies can offer new insights into various aspects of tumor evolution, such as the historical record of subclonal growth rates (i.e, "phylogenetic fitness") or the kinetics of tumor cell state transitions (which can be quantified as a "clonal plasticity" score for each cell). In our previous work, we described a model whereby KP-Tracer tumor progression is driven by the loss of an initial AT2-like cell state and accompanying increases in single-cell clonal plasticity and transcriptional heterogeneity; in turn, these high-plasticity cells provide a diverse pool of transcriptional states from which high-fitness, low-plasticity subclones with increased metastatic ability and expression for EMT markers like

306 *Vim* and *Hmga2* are selected[50]. Consistent with this previous work, the tumors studied with this
307 spatial-lineage platform showed an overall distribution where transient increases in plasticity are
308 followed by the selection of low-plasticity, high fitness subclones (**Figure S3A**). Using this
309 platform, we sought to understand how our previously described model unfolds spatially and
310 associates with changes to the surrounding microenvironment.

311 As the measurement of phylogenetic fitness reports on the history of subclonal growth,
312 spatially-resolved phylogenies are well suited to understanding the growth patterns in tumors and
313 their molecular consequences[22,68]. In one representative Slide-seq example (S-seq 40), we found
314 an expanding subclone with high phylogenetic fitness localized to a tumor interior characterized
315 by late-stage Hypoxic and EMT communities (C10 & C3) while the tumor periphery had lower
316 phylogenetic fitness and was marked by the Alveolar community (C1) (**Figure 3A**). This co-
317 localization of high phylogenetic fitness with hypoxic regions was supported by three lines of
318 evidence: first, we found that phylogenetic fitness was correlated with the orthogonal, previously-
319 described fitness signature[50] (Pearson's r = 0.4; **Figure S3B**). Second, in a systematic analysis
320 of all Slide-seq tumors, we found that the EMT and Hypoxic communities were most strongly
321 correlated with phylogenetic fitness (**Figure S3C**). Finally, across all high-resolution Slide-tags
322 arrays, we similarly found that the late-stage states (e.g., EMT and Endoderm-like) were most
323 likely to be found in regions that had previously undergone subclonal expansion (**Figure S3D**).
324 These orthogonal data collectively support the observation that the co-localization of expansion
325 and hypoxia is consistent across tumors and is not an artifact of tree reconstruction or the near-
326 cell resolution of Slide-seq.

327 The localization of expanding subclones characterized by aggressive gene expression
328 states in a representative Slide-seq example (S-seq 40) prompted us to hypothesize that rapid
329 subclonal expansions may create a layered environment whereby expanding subclones dominate
330 a core surrounded by non-expanding cells (**Figure 3A-B**). Focusing first on this representative
331 Slide-seq example, we observed that multiple low-fitness areas of Tumor 1 could be grouped
332 together in a phylogenetic subclade despite being geographically distant (though many indels
333 were shared across the tree, these low-fitness, distant cells were marked by the shared absence
334 of indels marking the expanding region) (**Figure 3A-B**; **Figure S3E**). Though this pattern could
335 be generated many ways (e.g., independent migration of several subclones), the most
336 parsimonious interpretation suggests that these scattered low-fitness cells were in close spatial
337 proximity during the early stage of tumor growth but were later pushed to the tumor periphery
338 because of a subclonal expansion event. To investigate the consistency of this phenomenon, we
339 next quantified the phylogenetic fitness of individual cancer cells derived from high-resolution

340 Slide-tags arrays on multiple tumors and inspected the spatial distribution of subclonal expansion.
341 In this analysis, we also found that the tumor core in Slide-tags data was more likely to contain
342 cells with more aggressive gene expression states (e.g., Endoderm-like and EMT states) and
343 higher phylogenetic fitness as inferred from reconstructed trees (**Figure 3C-D** $p < 1e\text{-}5$, wilcoxon
344 rank-sums test**; Figure 2C**; **Figure S2E**).

345 The observed data supporting a model in which subclonal expansion creates an
346 aggressive, hypoxic interior led us to next explore whether the transitions between gene
347 expression states also occur in a spatially coherent manner. As demonstrated in our previous
348 work, integrating high-resolution lineage tracing offers a unique opportunity to quantitatively
349 measure the frequency of cell state transitions, or "single-cell clonal plasticity"[50,69]. Starting in the
350 representative Slide-seq example (S-seq 40), we observed that low-plasticity clones in Tumor 1
351 co-localized with high-fitness regions in the tumor interior whereas the high-plasticity regions of
352 Tumor 2 (which lacked a subclonal expansion) appeared to lack spatial organization (**Figure 3A**).
353 Consistent with this, we found that the high-fitness Hypoxic and EMT communities, and related
354 states, were associated with lower plasticity across all Slide-seq and Slide-tags datasets (**Figure**
355 **S3F-G**). To better understand how transient increases in plasticity contribute to the subclonal
356 expansions observed across Slide-seq datasets (**Figure S3A**), we further examined the transition
357 to subclonal expansion in arrays profiled with Slide-tags (**Figure S4H-J**). Across our Slide-tags
358 data, we found there was little spatial organization of high-plasticity cells in tumors without
359 detectable subclonal expansion (as measured by Moran's *I* autocorrelation statistic[70]), whereas
360 low-plasticity cells were spatially localized to the tumor center in tumors after expansion (**Figure**
361 **S3I-J**; **Methods**). This suggests that subclonal expansion, and its associated molecular changes,
362 are important for coherent spatial organization during tumor progression.

363 Collectively, these data support a model whereby the tumor microenvironment is
364 sequentially remodeled by subclonal expansion, culminating in a hypoxic core and eventually the
365 emergence of a late-stage, pro-metastatic EMT state. As evidenced by examples of tumors across
366 various stages, this model is characterized by the exclusion of early-stage communities (e.g., C1:
367 Alveolar) to the tumor periphery while subclonal expansions contribute to the acquisition of a low-
368 plasticity, high-fitness Hypoxic community (C10) and eventual transition to an EMT community
369 (C3) (**Figure 3E; Figure 2F**; **Figure S2I**).

370

371 **Subclonal expansion is accompanied by immunosuppressive and fibrotic**
372 **microenvironmental remodeling**

373 As our Slide-seq data suggest that the microenvironment is remodeled during subclonal
374 expansion, we next exploited Slide-tags data to dissect the expansion-associated cell state
375 transitions at single-nucleus resolution. After quantifying phylogenetic fitness on trees inferred
376 from Slide-tags data, we stratified nuclei into high- and low-fitness groups and inspected the cell
377 type abundances in their spatial neighborhoods (**Figure 3F**; **Figure S3K**; **Methods**). As expected,
378 we found that the EMT cancer cell state was most consistently enriched in neighborhoods
379 surrounding high-fitness nuclei (**Figure 3F**). With respect to differential enrichment of specific
380 immune and stromal populations, we found that *Arg1*+ TAMs and myCAF populations were
381 consistently enriched in spatial neighborhoods of high-fitness cells whereas iCAFs and other
382 TAMs were not (**Figure 3F**). To more systematically probe the polarization states of macrophages
383 and fibroblasts associated with subclonal expansions, we performed differential expression within
384 these cell types in spatial neighborhoods of high- and low-fitness cells (**Figure 3G-H**). In addition
385 to high *Arg1* expression, macrophages in spatial neighborhoods of high-fitness cells were
386 characterized by the presence of the hypoxia-induced factor *Egnl3,* the Fcg-receptor *Fcgr2b,* the
387 macrophage scavenger receptor *Mrc1*, and enriched for programs indicating increased
388 endocytosis and complement activity (**Figure 3G; Table S1**). Fibroblasts associated with spatial
389 neighborhoods of high-fitness cells were characterized by higher expression of genes implicated
390 in hypoxia, collagen synthesis, and fibrosis such as *Vcan*, *Fndc1, Cald1* and *Vegfa* (**Figure 3H;**
391 **Table S1**).
392 To inspect the generalizability of these patterns, we returned to the comprehensive dataset
393 of 44 Slide-seq arrays. Indeed, a systematic analysis of our Slide-seq arrays revealed that spatial
394 neighborhood surrounding high-fitness, low-plasticity spots were most enriched for EMT, Hypoxic,
395 and Fibrotic communities (C3, C10, and C5, respectively) and depleted for Alveolar, Endothelial,
396 and Inflammatory communities (C1, C7, and C9, respectively) (**Figure S3L-M**; **Methods**).
397 Moreover, consistent with our finding in this mouse model, reanalysis of published spatial
398 transcriptomics data of human lung adenocarcinoma[40] demonstrated that expression of the
399 hypoxia-reporter *SLC2A1* (also known as *GLUT1*) in tumors was associated with cell proliferation
400 (as measured by *MKI67*), *TGFβ* signaling, EMT (*SNAI2*), and immunosuppressive macrophage
401 polarization (*FCGR2B)* (**Figure S3N-O**).
402 Together, these differential gene expression programs suggest a model whereby
403 subclonal expansion promotes a hypoxic tumor interior that polarizes immune and stromal cells
404 into pro-tumor immunosuppressive and fibrotic states and facilitates the emergence of a pro-
405 metastatic cancer cell state. Indeed, in returning to our previous Slide-seq analysis of community
406 program assignments across tumor progression, we observed that the Hypoxic community (C10)

407 appears prior to EMT (C3) when ranked by the transcriptional fitness signature (**Figure 2F; Figure**
408 **S2I**). In further support of this, immunofluorescence staining of KP-Tracer tumors revealed that
409 hypoxia (as evidenced by the canonical hypoxia marker GLUT1 [*Slc2a1]* protein levels[71,72])
410 preceded the emergence of immunosuppressive ARG1+ immune cells (**Figure 3I**).
411
412 **Spatially resolved lineages reveal the evolution of metastasis-initiating niches in the**
413 **primary tumor**
414 Metastasis, the ultimate stage of tumor progression, accounts for approximately 90% of
415 cancer-related mortality and is associated with pervasive microenvironmental remodeling[73–77].
416 However, it has remained challenging to delineate the specific microenvironmental features
417 associated with tumor evolutionary dynamics during metastasis progression. Outstanding
418 questions include: do the niches surrounding subclones giving rise to metastases differ from those
419 surrounding other subclones? How do these gene expression programs change during metastatic
420 spread? Our spatial-lineage platform is well-suited to identify the spatial localization of metastasis-
421 initiating subclones and characterize the microenvironmental remodeling associated with each
422 step of the metastatic cascade.
423 We began by performing spatial transcriptomics on a KP-Tracer mouse with multiple
424 primary lung tumors and widespread metastases in the mediastinal lymph node, rib cage, and
425 diaphragm (**Figure 4A, Figure S4A**). To maximize the probability of detecting metastasis-initiating
426 subclones in primary tumors, we sampled multiple representative layers of the tumor-bearing lung
427 at approximately 200-500um intervals, enabling us to study multiple large primary tumors from
428 top-to-bottom. Tumor segmentation of Slide-seq data from these sections and coarse-grained
429 spatial alignment determined by shared lineage states revealed four major tumors that could be
430 tracked across layers (**Figure 4B**).
431 Our spatial-lineages in the large Slide-seq assays provide an opportunity to both compare
432 the trajectory of multiple tumors and understand the transcriptional evolution of the niche
433 surrounding the metastasis-initiating subclone in a single primary tumor. To do so, we first
434 identified the spatial localization of subclones giving rise to metastasis by inspecting the allelic
435 similarities between primary tumors and metastases (**Figure 4C**). This analysis revealed that
436 metastases from all 3 locations were phylogenetically related to a spatially coherent subclone in
437 primary Tumor 2 ("T2"). T2 could be identified in each layer independently and could be thus
438 tracked across all sampled layers of this primary tumor (**Figure S4B-C**). This pattern was
439 consistent in matched Slide-tags data, overlapped with subclonal expansions identified from our
440 phylogenies, and was associated with regions exhibiting poorly differentiated histological features

441 (**Figure 4C-E; Figure S4C-F**). Because all metastases shared indels with an expanding subclone
442 that could be found across layers, it is most likely that all metastases arose after subclonal
443 expansion.
444 To understand the phylogenetic and gene expression programs underlying metastatic
445 potential in this region of T2, we segmented this tumor into a niche surrounding the cells giving
446 rise to metastases ("T2-Met") or otherwise ("T2-NonMet") and compared their gene expression
447 patterns (**Figure 4D-E; Figure S4D-F**; **Methods**). The T2-Met niche had higher proportions of the
448 EMT and Hypoxic communities (C3 & C10, respectively) and lower proportions of the
449 Gastric/Endoderm and Alveolar communities (C11 & C1, respectively) (**Figure 4F**). The T2-Met
450 niche additionally down-regulated genes associated with Gastric and Endoderm states (e.g.,
451 *Gkn2* and *Meg3*), and had higher expression of genes marking cancer cell EMT (e.g., *Vim*),
452 scavenger macrophages (e.g., *Mrc1* and *Msr1*), immunosuppressive macrophages (e.g., *Arg1*
453 and *Fcgr2b*), TGFβ signaling (e.g., *Tgfb1* and *Smad4*), and fibrosis (e.g., *Cthrc1* and *Postn*)
454 (**Figure 4G**). Orthogonal analysis with Slide-tags data corroborated these findings, as *Arg1*+
455 TAMs and myCAFs were most enriched in spatial neighborhoods of cells in the primary tumor
456 related to metastases (**Figure S4G**). Moreover, immunofluorescence staining confirmed that
457 ARG1+ cells co-localized with the metastasis-initiating VIM+ region of the T2 primary tumor
458 (**Figure S4H**). Together, these results nominate several key molecular processes as potential
459 drivers of the pro-metastatic niche, including fibrosis, TGFβ signaling, and intercellular
460 interactions between cancer cells, activated fibroblasts, and *Arg1*+ immunosuppressive
461 macrophages.
462
463 **Metastatic colonization is accompanied by increased collagen deposition and fibrosis**
464 Beyond the evolution within the primary tumors, we next investigated whether the
465 microenvironments at distant metastatic sites are remodeled to resemble, or diverge from, the
466 metastasis-initiating niche within the primary tumor. Comparing the niches surrounding
467 metastases and the T2-Met subclone in the primary tumor, we found that metastases contained
468 proportionally more regions annotated by stromal or immune communities and showed
469 specifically higher representation of the Fibrotic community (C5) (**Figure 4F**). As these
470 communities represent several gene programs and may mask fine-scaled cell type changes, we
471 further characterized the differential gene expression changes distinguishing niches of the primary
472 tumor and metastases (**Figure 4G**). While metastases up-regulated genes also found to
473 distinguish the T2-Met niche – such as the EMT markers *Vim* and *Hmga2* and TGFβ-related
474 genes – metastases displayed large up-regulation of genes associated with collagen deposition

475 (e.g., *Col1a1* and *Col12a1*) and myogenesis (*Tnnt3* and *Ncam1*) (**Figure 4G**). After quantifying
476 the activity of these gene expression programs in Slide-seq spots, we confirmed that these
477 aggregated gene expression signals were spatially localized to tumor regions: metastatic tumors
478 generally resembled the metastasis-initiating subclone in the primary tumor (for example with
479 respect to TGFβ signaling: log2FC = -0.14, t-test p=1.0; **Figure 4H**) but substantially up-regulated
480 collagen-related genes as compared to the primary tumor (log2FC = 3.81, t-test $p<1e-5$) (**Figure**
481 **4I**). Consistent with this finding in Slide-seq data, immunofluorescence staining showed a marked
482 increase in COL3A1 protein in metastases as compared to primary tumors **(Figure S4I**).
483 Collectively, these results complement recent findings that TGFβ signaling is critical for EMT and
484 metastatic seeding in this model[74], and highlight that while certain expression programs – such
485 as TGFβ signaling – precede metastasis in the metastasis-initiating subclone, the resulting
486 metastatic tumor is remodeled to have increased fibrosis and collagen-related gene program
487 activity.
488
489 **DISCUSSION**
490 In this study, we integrated high-resolution spatial transcriptomics with Cas9-based
491 lineage tracing in a genetically engineered mouse model of lung adenocarcinoma to dissect the
492 dynamic interplay between tumor evolution and microenvironmental remodeling in a spatially
493 resolved fashion. Our analysis uncovered spatial communities associated with different stages of
494 tumor progression; revealed relationships between tumor growth, plasticity and
495 microenvironmental remodeling; and identified metastasis-initiating subclones that informed on
496 the spatiotemporal evolution of gene expression along the metastatic cascade. These results
497 present an unprecedented spatial map of lung adenocarcinoma evolution, showcasing the power
498 of integrating spatially resolved transcriptomics and lineages to dissect the complex tumor
499 dynamics underlying cancer progression.
500 The insights into spatiotemporal dynamics offered by this spatial-lineage platform
501 contributes new dimensions to our previous model of KP tumor evolution (**Figure 4J)**. Our
502 previous results provided several lines of evidence that tumors, following the initial loss of an AT2-
503 like state, are characterized by a cancer-cell-intrinsic increase in clonal plasticity, leading to gains
504 in transcriptional heterogeneity and subsequent subclonal expansion[50]. In the present study, we
505 find that rapid subclonal expansion pushes early-stage cells to the tumor periphery and
506 contributes to the formation of a hypoxic microenvironment in the tumor core. This hypoxic niche
507 promotes additional microenvironmental remodeling characterized by *Arg1*+ immunosuppressive
508 myeloid subsets and myCAF-like fibroblasts; for example, by recruiting myeloid cells through

509 hypoxia-induced chemokine secretion (e.g., *Ccl2, Ccl6,* and *Csf1*) and polarizing immune and
510 stromal cells through hypoxia-induced signaling cascades (e.g., *Hif1a* and *Vegfa*) as previously
511 suggested[78–82] (**Figure S2A,G; Figure 3G-H**). In turn, this hypoxic, immunosuppressive, and
512 fibrotic niche may contribute to another wave of cancer cell state transitions and the emergence
513 of a pro-metastatic EMT state, for example through *TGFβ* signaling as shown in our analysis
514 (**Figure 4G-H**) and detailed in a recent study[74]. As these cells metastasize, the metastatic
515 environment is further remodeled to an enhanced fibrotic niche marked by increased collagen
516 deposition.

517 Epigenetic remodeling is a hallmark of cancer and has been shown to play a critical role
518 in cancer progression and drug resistance[83–85]. Our proposed model of tumor progression
519 provides key insights into how cancer-intrinsic alterations and external signals integrate to
520 regulate tumor cell states. Building on previous work in this model which has shown that tumor
521 progression is driven by epigenetic rather than somatic changes[50,54], our analysis adds more
522 granularity into this process and suggests an appealing hypothesis that epigenetic remodeling
523 can be disentangled into two distinct phases. First, following the loss of the AT2-like state, cancer
524 cells enter a permissive epigenetic phase characterized by increased plasticity and transcriptional
525 heterogeneity. As high-plasticity regions of these tumors do not appear to be spatially coherent
526 (**Figure 3A, Figure S3H-I**), this suggests that this phase of epigenetic remodeling is mostly driven
527 by cell-intrinsic changes accompanying the loss of the AT2-like state.

528 In contrast, the second phase of epigenetic changes follows subclonal expansions that
529 drive microenvironmental remodeling towards a hypoxic state characterized by
530 immunosuppressive and fibrotic communities. As several lines of evidence suggest that hypoxia
531 precedes the formation of the EMT state (**Figure 2F, Figure S2I, Figure 3E**), we postulate that
532 these environmental changes contribute to the induction and selection of an epigenetically-stable,
533 pro-metastatic EMT state. This hypothesis aligns with prior reports associating hypoxia with
534 genomic instability and EMT[22,86–88], including in human lung adenocarcinoma[89], and here our
535 spatial-lineage data provide new evidence linking subclonal expansion as a mechanism driving
536 hypoxia and tumor progression. In addition to our observation that human lung adenocarcinoma
537 tumors contain spatially-defined hypoxic regions[90] (**Figure S3N-O**), hypoxia has also been shown
538 to play critical roles in lung adenocarcinoma[91] and other cancers (e.g., glioma[92] and clear cell
539 renal cell carcinoma[22]); thus, further dissecting the relationships between subclonal expansions
540 and hypoxia in these cancers may reveal opportunities for therapies spanning multiple cancer
541 types. Together, these findings provide fundamental insights into how cancer cell states are

542 regulated by both intrinsic and extrinsic changes and highlight the possible therapeutic
543 ramifications of this regulation.
544 While our study elucidates new aspects of how tumor evolution unfolds spatially, it also
545 sets the foundation for further studies. First, mechanistic studies will be needed to dissect how
546 the hypoxic niche polarizes immune and stromal subsets, and how this might lead to an
547 aggressive, mesenchymal tumor state. As we have previously reported that plasticity plays an
548 important role in tumor progression[28,50,55,83], one area of research will be how hypoxia affects the
549 high-plasticity cell states in lung cancer. Second, the platform we developed here can be adapted
550 to study the spatiotemporal dynamics of tumor evolution in other models or under different
551 perturbations. Notably, our platform is also amenable to modeling the effect of additional genetic
552 perturbations as Cas9 is continuously expressed for tracing[50]. Third, while we introduced new
553 computational approaches for phylogenetic reconstruction approaches that address the sparsity,
554 resolution, and scale of these data, there remain opportunities to build new algorithms specifically
555 tailored to the spatial aspect of data and statistically infer how spatial organization affects
556 phylogenetic patterns.
557 In summary, our study unites the insights provided by spatially resolved lineages and
558 transcriptomics to investigate the fundamental patterns of tumor growth and its interactions with
559 the microenvironment. Our analyses lead to a comprehensive model of how a tumor grows from
560 a single, transformed cell into a large and complex ecosystem and provided new evidence for
561 how tumor expansion-associated microenvironmental remodeling may contribute to a distinct
562 wave of cell state reprogramming towards pro-metastatic states. As one of the most
563 comprehensive datasets of spatial tumor evolution to date, we anticipate that this resource will
564 help pioneer new computational methods and quantitative and predictive models of tumor
565 evolution.
566
567 **Limitations of the study**
568 While our study reveals new aspects of tumor progression, there are limitations in the
569 interpretation and extensibility of the approaches applied here. First, a single slide section may
570 not represent the entirety of clonal dynamics in a tumor. To minimize this potential bias, we
571 corroborated phylogenetic patterns with histology, orthogonal gene expression signatures derived
572 from our previous single-cell lineage-tracing data (derived from unbiased sampling of whole
573 tumors) and analyzing representative sections at different depths of tumors from a tumor-bearing
574 lung in **Figure 4**. As scaling spatial transcriptomics experiments becomes more affordable, future
575 studies can more densely sample three-dimensional structure to entirely account for this bias.

576 Second, as a consequence of profiling tumor sections, we observe less indel diversity in spatial
577 lineage tracing data than in previous applications with unbiased sampling, leading to lower
578 resolution phylogenetic relationships. This may be ameliorated by optimizing the lineage-tracing
579 kinetics and adapting tools for recording past molecular signaling events[93,94]. Third, the molecular
580 sparsity and resolution of Slide-seq data pose a challenge in reconstructing phylogenies and
581 detecting smaller spatial neighborhoods. While we provide a spatial imputation algorithm to
582 account for these technical issues, and benchmark its effectiveness in a variety of simulated and
583 held-out experiments, we anticipate that this imputation approach may have limitations in cases
584 where lineage data is not spatially coherent, for example in systems with higher degrees of cell
585 migration. In these scenarios, either alternative technologies with improved capture and resolution
586 or new algorithms for performing spatial imputation and detecting robust spatial communities will
587 be necessary. Finally, the trees presented in this study are only estimates of true phylogenetic
588 relationships, and may not truly reflect cell division histories; when possible, our study uses
589 orthogonal data and approaches to substantiate all claims.
590

591 **ACKNOWLEDGEMENTS**

592 We thank Jack Rose, Can Ergen, Chen Weng, Pu Zheng, Sean-Luc Shanahan, Yun
593 Zhang, Anjali Saqi, Meaghan McGery, Santiago Naranjo, Michelle Chan, Romain Lopez, Adam
594 Gayoso, and all members of the Weissman, Yang, Yosef, Chen, and Chang labs for helpful
595 discussions. We thank Cristen Muresan, Anne Odera, Maria Gould, Daniel Braslavsky, Maxim
596 Litvinov, and Nicole Dow for administrative support. We thank the Whitehead Institute and Broad
597 Institute Sequencing Facility for sequencing support.

598 M.G.J. is supported by an NCI Pathway to Independence Award (NIH K99CA286968).
599 N.M.A. was supported by a NIH F30 fellowship (1F30CA278495). K.E.Y. was supported by the
600 National Cancer Institute of the National Institutes of Health under Award Number K00CA253729.
601 L.W.K. is supported by a Helen Hay Whitney Postdoctoral Fellowship. T.J. laboratory currently
602 also receives funding from The Lustgarten Foundation for Pancreatic Cancer Research, but this
603 funding did not support the research described in this manuscript. This work was supported in
604 part by the Cancer Center Support (core) grant P30-CA14051 from the National Cancer Institute
605 and by the NIH grant R35CA274464. T.J. is the David H. Koch Professor of Biology and a Daniel
606 K. Ludwig Scholar. J.S.W. is supported by the Howard Hughes Medical Institute, NCI Cancer
607 Target Discovery and Development (CTD^2) and NIH Centers of Excellence in Genomic Science
608 (CEGS). Both J.S.W. and T.J. received fundings from Ludwig Center at MIT. D.Y. is supported
609 by a Damon Runyon Dale Frey Award, an NCI Transition Career Development Award

1K22CA289207 and an NIH Director's New Innovator Award 1DP2OD037078. N.Y. is supported in part by an NIH grant R56-HG013117 and by the European Union Council (ERC, Tx-phylogeography, 101089213). Views and opinions expressed are however those of the authors only and do not necessarily reflect those of the European Union or the European Research Council Executive Agency. Neither the European Union nor the granting authority can be held responsible for them. F.C. acknowledges support from NIH Early Independence Award (DP5, 1DP5OD024583), the NHGRI (R01, R01HG010647), the Burroughs Wellcome Fund CASI award, the Searle Scholars Foundation, the Harvard Stem Cell Institute, and the Merkin Institute. This research was supported by the NYSCF. FC is a New York Stem Cell Foundation – Robertson Investigator

AUTHOR CONTRIBUTIONS

D.Y., J.S.W., N.Y., F.C. and K.H.(J.)M. conceived of the project. D.Y., L.T, and D.S. transduced mice, sacrificed mice, harvested tumors, and constructed spatial transcriptomics sequencing libraries. W.M.R III generated the KP-Tracer chimeric mice. M.G.J. analyzed the lineage-tracing and gene expression spatial transcriptomics data with help from K.H.(J.)M., W.N.C, and V.Z.C. M.G.J. and K.H.(J.)M. performed simulation benchmarks for Slide-seq data with input from W.N.C., L.W.K., and K.E.Y. J.W. performed spatial-mapping of Slide-tags data. D.S. and N.M.A. performed staining and imaging of H&E and immunofluorescence and histology analysis. D.Y., M.G.J., D.S., T.J., J.S.W., N.Y., and F.C. interpreted the results. M.G.J., D.Y., and D.S. wrote the manuscript with input from all authors.

DECLARATION OF INTERESTS

M.G.J. consults for and has equity in Vevo Therapeutics. K.E.Y. is a consultant for Cartography Biosciences. T.J. is a member of the Board of Directors of Amgen and Thermo Fisher Scientific, and a co-Founder of Dragonfly Therapeutics and T2 Biosystems. T.J. serves on the Scientific Advisory Board of Dragonfly Therapeutics, SQZ Biotech, and Skyhawk Therapeutics. T.J. is the President of Break Through Cancer. None of these affiliations represent a conflict of interest with respect to the design or execution of this study or interpretation of data presented in this manuscript. J.S.W. declares outside interest in 5 AM Venture, Amgen, Chroma Medicine, KSQ Therapeutics, Maze Therapeutics, Tenaya Therapeutics, Tessera Therapeutics, Ziada Therapeutics, DEM Biopharma, and Third Rock Ventures. D.Y. declares outside interest in DEM Biopharma.

DATA AND CODE AVAILABILITY

Custom code for the analysis of spatially-resolved lineage-tracing data is available on Github through Cassiopeia (https://github.com/YosefLab/Cassiopeia) and at https://github.com/mattjones315/KPSpatial-release. All raw and processed data will be made available on GEO and other public repositories.

SUPPLEMENTARY TABLES

Table S1: Fitness-neighborhood differential expression and GO Term analyses.

METHODS

EXPERIMENTAL MODELS AND SUBJECT DETAILS

KP-Tracer mouse was generated by generating chimeric mice from blastocyst injection of engineered, lineage tracer enabled mouse embryonic stem cells harboring conditional alleles *Kras*$^{LSL\text{-}G12D/+}$;*Trp53*$^{fl/fl}$; *Rosa26*$^{LSL\text{-}Cas9\text{-}P2A\text{-}mNeonGreen}$ as previously described[50]. Eight-to-twelve-week-old KP-Tracer mice were infected intratracheally with ad5-SPC-Cre virus (1x10^8 Pfu) purchased from University of Iowa viral vector core for tumor initiation. This enables specific tumor initiation and lineage-tracing in Alveolar Type II (AT2) cells, the major cell-type of origin of lung adenocarcinoma. All studies were performed under an animal protocol approved by the Massachusetts Institute of Technology (MIT) Committee on Animal Care. Mice were assessed for morbidity according to MIT Division of Comparative Medicine guidelines and humanely sacrificed prior to natural expiration.

METHODS DETAILS

Sample processing

Tumor-bearing lungs were harvested and re-inflated with ~2ml of 50% OCT (1:1 mix with PBS) and 1:100 of RNase inhibitor (NEB M0314L). After cleaning up excess blood and liquid, the whole tissue was embedded in 100% OCT and frozen using dry ice-methanol bath. Frozen samples were kept at -80C until sectioning for further analysis.

Spatial transcriptomics with Slide-seqV2

For 3 mm and 5.5 mm arrays. Fresh frozen tissues were cryo-sectioned at a thickness of 10 μm using a Cryostat (CM1950, Leica) set at −17 to −18 °C. The tissue sections were carefully transferred onto precooled arrays, which were placed on top of a glass slide inside the cryostat. A finger was briefly placed underneath the slide to melt the tissue and adhere it to the array. Immediately after, the tissue and array were transferred together into a 1.5 ml or 2 ml

677 Eppendorf tube containing 200 µl (for 3 mm arrays) or 500 µl (for 5.5 mm arrays) of hybridization
678 buffer (6x SSC with 2 U μl^{-1} Lucigen NxGen RNase inhibitor, Lucigen, 30281). The samples were
679 incubated in the hybridization buffer for 15 minutes to 1 hour at room temperature, allowing the
680 RNA to bind to the oligonucleotides on the beads. After incubation, the tissue and array were
681 briefly dipped into 1x Maxima RT buffer to wash off the hybridization buffer and then transferred
682 to the reverse transcription (RT) reaction mixture (1x Maxima RT buffer, 1 mM dNTPs (NEB,
683 N0477L), 2 U μl^{-1} Lucigen NxGen RNase inhibitor, 2.5 µM template switch oligonucleotide, 10
684 U/µL Maxima H Minus reverse transcriptase (Thermofisher Scientific, EP0753)). The tissue and
685 array were incubated in 200 µl (for 3 mm arrays) and 500 µl (for 5.5 mm arrays) of the RT reaction
686 mixture for 30 minutes at room temperature, followed by 1.5 hours at 52 °C. To digest the tissue,
687 200 µl (for 3 mm arrays) or 500 µl (for 5.5 mm arrays) of tissue digestion buffer (200 mM Tris-Cl
688 pH 8, 400 mM NaCl, 4% SDS, 10 mM EDTA and 32 U ml^{-1} proteinase K (NEB, P8107S)) was
689 added to the reaction mixture and incubated at 37 °C for 30 minutes. Following digestion, 200 µl
690 (for 3 mm arrays) or 500 µl (for 5.5 mm arrays) of wash buffer (10 mM Tris pH 8.0, 1 mM EDTA
691 and 0.01% Tween-20) was added, and a P200 pipette was used to carefully triturate the beads
692 off the array. The beads were centrifuged at 3000g for 2 minutes, followed by three washes with
693 wash buffer. To remove RNA strands, the beads were incubated in 0.1N NaOH for 5 minutes,
694 followed by a wash with wash buffer and 1x TE buffer, and centrifuged again at 3000g for 2
695 minutes. Second-strand synthesis was performed by mixing the beads with 200 µl (for 3 mm
696 arrays) or 500 µl (for 5.5 mm arrays) of second-strand synthesis mixture (1x Maxima RT buffer,
697 1 mM dNTPs, 10 µM dN-SMRT oligonucleotide and 12.5U μl^{-1} Klenow enzyme (NEB, M0210))
698 and incubating at 37 °C for 1 hour. The beads were then washed three times with wash buffer
699 and once with water. cDNA amplification was carried out by resuspending the beads in 200 µl (for
700 3mm arrays) or 1.2 ml (for 5.5 mm arrays) of cDNA amplification mixture (1x Terra Direct PCR
701 mix buffer (Takara Biosciences, 639270), 1.25 U μl^{-1} of Terra polymerase (Takara Biosciences,
702 639270), 2.5 µM TruSeq PCR handle primer and 2.5 µM SMART PCR primer). The reaction was
703 divided into 50 µl aliquots and amplified using the following PCR program: 95 °C for 3 min; four
704 cycles of 98 °C for 20 s, 65 °C for 45 s and 72 °C for 3 min; nine cycles of 98 °C for 20 s, 67 °C for
705 20 s and 72 °C for 3 min; 72 °C for 5 min; hold at 4 °C. The cDNA product was purified twice using
706 SPRI beads (Beckman Coulter, B23318) at a 0.8x bead-to-sample ratio, eluting in a final volume
707 of 20 µl (for 3mm arrays) and 60 µl (for 5.5 mm arrays). A total of 1 ng (for 3 mm arrays) or 3x 1ng
708 (for 5.5 mm arrays) of cDNA was used for Illumina sequencing library construction. The Nextera
709 XT kit (Illumina, FC-131-1096) was used for tagmentation, followed by amplification with TruSeq5
710 and N700 series barcoded index primers. Libraries were cleaned with SPRI beads according to

711 the manufacturer's instructions at a 0.6x bead-to-sample ratio and resuspended in 10 µl of water
712 per reaction. Lineage tracing target site libraries were amplified from cDNA and prepared fpr
713 Illumina sequencing using previously described protocols[50].
714 ***For Curio 1 cm arrays.*** The buffers and enzymes used were the same as those described
715 for the 3 mm and 5.5 mm arrays but adjusted for scale. In brief, hybridization, dipping, washing,
716 RT reaction and tissue digestion were performed using the reservoirs provided by Curio with 500
717 µl volume for each step. After tissue digestion the beads were divided into 2 tubes for wash buffer
718 washes and combined for cDNA amplification. A total of 4.8 ml of cDNA amplification mixture was
719 prepared, and the reaction was divided into 50 µl aliquots for cDNA amplification in 96-well PCR
720 plates, following the same PCR program as outlined previously. cDNA was purified twice using
721 0.8x SPRI beads and eluted in a final volume of 80 µl. 8x 1ng cDNA products were used for
722 Illumina sequencing library preparation through tagmentation with a Nextera XT kit, followed by
723 amplification and cleanup as stated above. Lineage tracing target site libraries were amplified
724 from cDNA and prepared fpr Illumina sequencing using previously described protocols[50].
725
726 **Spatial transcriptomics with Slide-tags**
727 Fresh frozen tissues were cryo-sectioned at 20 µm thickness using a Cryostat set at −17
728 to −18 °C. Precooled 6 mm square custom-made biopsy punches were used to punch and isolate
729 regions of interest from the tissue sections. The isolated tissue regions were carefully transferred
730 onto a precooled array, which was placed on top of a glass slide. A finger was briefly placed
731 underneath the slide to melt the tissue onto the array. Immediately after, the tissue, array, and
732 slide were placed on ice, and approximately 10 µl of dissociation buffer (82 mM Na_2SO_4, 30 mM
733 K_2SO_4, 10 mM glucose, 10 mM HEPES, 5 mM $MgCl_2$) was gently pipetted onto the tissue to
734 ensure it was fully covered. The array was then exposed to an ultraviolet (UV) light source (0.42
735 mW mm^{-2}, Thorlabs, M365LP1-C5, Thorlabs, LEDD1B) for 1 minute to cleave spatial barcode
736 oligonucleotides off the beads. After photo-cleavage, the array was incubated on ice for 7.5
737 minutes before being transferred to a well of a 12-well plate. To release the tissue from the array,
738 1 ml of extraction buffer (dissociation buffer with 1% Kollidon VA64, 0.2% Triton X-100, 1% BSA,
739 666 U ml^{-1} RNase-inhibitor) was gently dispensed onto the array, and the buffer was carefully
740 triturated up and down over the tissue 10–15 times. This process was repeated until the tissue
741 was completely released from the array. The array was then discarded, and mechanical
742 dissociation of the tissue was performed by triturating the supernatant 100–150 times using a 1
743 ml pipette to fully release the nuclei from the tissue. The extraction buffer containing the nuclei
744 was transferred to a 15 ml tube. The well was washed three times with 1 ml of wash buffer

745 (dissociation buffer with 1%BSA and 1: 100 RNase-inhibitor) and the washes were pooled into the
746 same 15 ml tube. The final volume of the wash buffer was adjusted to 10 ml. The nuclei were
747 centrifuged at 600g for 10 minutes at 4 °C. After centrifugation, 9.5 ml of the supernatant was
748 carefully removed. The pellet was resuspended and passed through a precooled 40 μm cell
749 strainer (Corning, 431750) into a 1.5 eppendorf tube. The 15 ml tube and cell strainer were
750 washed with 1 ml of wash buffer, and the nuclei were pelleted again by centrifuging at 600g for
751 10 minutes at 4 °C. After centrifugation, the supernatant was carefully removed, leaving
752 approximately 50 μl of wash buffer for nuclei resuspension. To determine cell count, 2 μl of
753 resuspended nuclei was mixed with 18 μl of 1: 100 diluted DAPI, and the nuclei were manually
754 counted using a C-Chip Fuchs-Rosenthal disposable hemocytometer (INCYTO, DHC-F01-5).
755 Based on the cell count, up to 25,000 nuclei were processed using the Chromium Next GEM
756 Single Cell 3' Reagent Kits v3.1 (with Feature Barcode technology for Cell Surface Protein, 10x
757 Genomics, PN-1000268). Lineage tracing target site libraries were amplified from cDNA and
758 prepared fpr Illumina sequencing using previously described protocols[50].
759
760 **H&E staining**
761 H&E was performed with a Leica ST5010 Autostainer XL and Leica CV5030 Fully
762 Automated Glass Coverslipper. Bright-field images were taken using the Leica Aperio VERSA
763 Brightfield, Fluorescence & FISH Digital Pathology Scanner under a ×10 objective. Tumor grade
764 was analyzed in H&E-stained sections using an automated deep neural network developed by
765 Aiforia.
766
767 **Sequencing**
768 Sequencing was performed at using NovaSeq S4. For Slide-seq gene expression libraries:
769 read1: 50bp, read2: 50bp, index1: 8bp was used. For Slide-seq Target Site libraries: read1: 44bp,
770 read2: 260bp, index1: 8bp was used. For Slide-tags gene expression libraries: read1: 28bp,
771 read2: 90bp, index1: 10bp, index2: 10bp was used. For Slide-tags gene expression libraries:
772 read1: 28bp, read2: 260bp, index1: 8bp setting was used.
773
774 **Immunofluorescence staining & imaging**
775 15 μm-20 μm tissue sections were fixed in 4% PFA at room temperature for 10-15 min.
776 The sections were washed twice in 1x PBS. Antigen retrieval was performed by boiling 1X IHC
777 Antigen Retrieval Solution (ThermoFisher Scientific, 00-4955-58) and incubating tissue sections
778 inside for 30 min until the solution cooled down, followed by washing tissue sections with 1x PBS

779 and incubated in 0.3% PBST (0.3% Triton X-100 in PBS) at room temperature for 10 min. Three
780 times of 1x PBS wash was then performed. Blocking (0.5% BSA and 0.1% Triton X-100 in 1x
781 PBS) was performed at room temperature for 1 hour. Tissue sections were incubated with primary
782 antibodies: VIM (1: 200, Biotechne, AF2105), CD31 (1: 200, Biotechne, AF3628), ARG1 (1: 200;
783 Cell Signaling Technology, 93668), GLUT1 (1: 100; AbCam, ab195020), CD45 (1: 200, Cell
784 Signaling Technology, 70257), and COL3A1 (1: 200, Proteintech, 22734-1-AP) at 4 °C overnight.
785 Tissue sections were washed three times with 1x PBS and further incubated with secondary
786 antibodies (donkey anti-goat 405, 1: 1000, ThermoFisher Scientific, A-48259; donkey anti-mouse
787 647, 1: 1000, ThermoFisher Scientific, A-31571; donkey anti-rabbit 647, 1: 1000, ThermoFisher
788 Scientific) at room temperature for 2-3 hours. Tissue sections were then washed three times with
789 1x PBS, mounted and imaged using Dragonfly 201-40 High Speed Confocal Imaging Platform.
790

791 **QUANTIFICATION AND STATISTICAL ANALYSIS**

792 **Slide-seqV2 gene expression quantification and quality-control**

793 A python implementation of Kallisto-bustools[95] (*kb_python,* version 0.27.3 available at
794 https://github.com/pachterlab/kb_python) was used for transcript quantification and processing
795 from raw FASTQs produced with Slide-seq. Specifically, we utilized the *count* procedure
796 implemented in Kallisto that quantifies the number of UMIs in a Slide-seq library that map to each
797 transcript sequence in the provided reference (here, *mm10*). To account for the unique read
798 structure of the Slide-seq library, we invoked the *count* procedure with the flag -x
799 "0,0,8,0,26,32:0,32,41:1,0,0". To determine a whitelist of barcodes to use during quantification,
800 we matched barcodes identified with kallisto to the spatial barcodes and their coordinates
801 observed during *in situ* sequencing of the Slide-seq array during fabrication[56,57]. We then used a
802 custom script to assign spatial coordinates, identified during *in situ* sequencing of the Slide-seq
803 array prior to running the assay, to quantifications from the kallisto pipeline and returned an
804 AnnData structure containing the spatially-resolved transcript abundances for each spot. To
805 supplement the barcode filtering during the kallisto pipeline, we applied an extra filter requiring at
806 least 150 UMIs observed in a spot. For most analyses, we utilize log-normalized counts where
807 each cell's UMI total is scaled to the median library size and a log1p transformation is applied.
808 When scaled counts are used, we additionally use Scanpy's *scale* function with a max value of
809 10.
810

811 **Slide-tags gene expression quantification and quality-control**

Similar to Slide-seq processing, we utilized the python implementation of Kallisto-bustools[95] (*kb_python,* version 0.27.3 available at https://github.com/pachterlab/kb_python) to quantify transcript abundance from FASTQ data. As this data represents reads from sequencing single-nuclei with the 10X V3 kit, we utilized the *--umi-gene*, *--workflow nucleus*, and *-x 10XV3* flags. Similar to the Slide-seq analysis, we utilized the mm10 transcriptome reference.

After transcript quantification, we applied several quality-control procedures. First, we removed background gene expression signal from ambient RNA by applying Cellbender[96] (version 0.3.0, available at https://github.com/broadinstitute/CellBender) to the unfiltered gene expression counts. We used default settings for all libraries, except for 10X Library 9 where we used the following flags: --empty-drop-training-fraction 0.15, --total-droplets-included 20000, --learning-rate 0.0001, and --epochs 300. After running Cellbender, we applied further cell-filters to remove outliers with high mitochondrial or ribosomal content (between 5-15% for libraries). We further inspected the count distribution in each library and removed nuclei with excessively high UMI content (approximately 20,000 UMIs). All quality-control was performed with Scanpy[97] (version 1.10.0, downloaded via *pip*). For most analyses, we utilize log-normalized counts where each cell's UMI total is scaled to the median library size and a log1p transformation is applied. When scaled counts are used, we additionally use Scanpy's *scale* function with a max value of 10.

Slide-seq lineage tracing target-site data processing

To begin processing target-site data, we trimmed reads from Slide-seq libraries using cutadapt[98] (version 4.1) with the following flags: -m :250 --max-n 0.2 --discard-untrimmed -O 10 --no-indels --match-read-wildcards -e 2 -j 16 --action retain -G AATCCAGCTAGCTGTGCAGC. We then applied Cassiopeia[41] (version 2.0.0, available at https://github.com/YosefLab/Cassiopeia) to trimmed FASTQs using the "slideseq2" chemistry and specific parameters for Slide-seq libraries. First, to account for the possibility of multiple cells observed in a given spot, we allowed allele conflicts (*allow_allele_conflicts* = *True*) and did not enable doublet filtering. While we performed intBC whitelist correction, we did not perform additional error correction to remove intBCs with conflicting alleles (this is similarly motived by the fact more than one cell can be observed in a given spot). We additionally relaxed the UMI/cell threshold to account for reduced capture of Slide-seq assays (*min_umi_per_cell* = *2*). Finally, we utilized the "likelihood" method for UMI collapsing, with *max_hq_mismatches* = 3 and *max_indels* = 2. Other settings remained default. This pipeline produced a cleaned allele table, reporting the set of intBCs and alleles for each observed spot, that was used for tree reconstruction.

846

847 **Slide-tags lineage tracing target-site data processing**

848 Cassiopeia[41] (version 2.0.0, available at https://github.com/YosefLab/Cassiopeia) was used to
849 process FASTQs containing target-site data. As Slide-tags represents single-nucleus data, we
850 utilized default settings except for a more relaxed UMI/cell cutoff (*min_umi_per_cell = 5)* to reflect
851 the reduced sensitivity of single-nucleus sequencing. As a part of default settings, we corrected
852 cell barcodes to those observed after quality-control filtering, corrected intBCs to a whitelist for
853 the corresponding mESC (E1) with a distance threshold of 1, and performed UMI (with a maximum
854 distance of 2) and intBC error correction (minimum UMI support of 5) to correct for conflicting
855 target sites observed in the same nuclei. Doublets were filtered out using the default conflicting
856 threshold of 35%. This pipeline produced a cleaned allele table, reporting the set of intBCs and
857 alleles for each observed spot, that was used for tree reconstruction.

858

859 **Slide-tags spatial barcode processing**

860 Spatial mapping of Slide-tags nuclei was achieved as previously described[58]. Briefly, reads from
861 spatial barcode FASTQ files were filtered for those containing the spatial barcode universal primer
862 constant sequence and cell barcode sequences from a called cell barcode whitelist generated by
863 the gene expression pipeline (see above section entitled "Slide-tags gene expression
864 quantification and quality-control"). Spatial barcode sequences were matched with a whitelist of
865 in situ sequenced spatial barcodes, assigning spatial coordinates to each true spatial barcode.
866 The set of spatial barcodes and the corresponding x,y coordinates for each cell barcode were
867 clustered with DBSCAN[99] (implemented in the R package *dbscan*, version 1.1−11). For cell
868 barcodes with a single cluster of spatial barcodes, spatial barcodes not contained in the cluster
869 were filtered out and a UMI-weighted centroid of the remaining spatial barcodes represented the
870 x,y coordinates of the cell barcode. DBSCAN parameters were determined from a sweep of
871 minPts values (3 to 15) under a constant eps = 50. The chosen minPts positioned the highest
872 proportion of cell barcodes.

873

874 **Spatial imputation of lineage-tracing data**

875 To recover lineage-tracing data for reconstruction on spatial assays, we performed
876 spatially-informed imputation of target site data. To begin, we first created a character matrix from
877 the allele tables constructed from target-site lineage tracing processing. In this character matrix,
878 denoted as X, each row corresponds to a cell (or spot) and each column corresponds to a
879 particular cut site in an integration barcode (intBC). For clarity of notation, we refer to each cut-

site/intBC pair as a character, and thus in our system a character matrix will have (|intBCs| x 3) columns. The entry $X[i,j]$ denotes the edit (which we refer to as a "state") observed at the ith cell/spot in the jth character. The missing data rate refers to the proportion of entries in this character matrix that do not have data that pass our quality-control filters.

To perform spatial imputation, we first constructed a spatial nearest-neighbor graph (N) such that each spot was connected to all other spots within 30μm of the spot. For each missing entry in character matrix, i,j we queried the frequency of states at character j in all neighbors of spot i in N. If the concordance of a particular state was higher than 80% in these neighbors, then we replaced the entry $X[i,j]$ with this state. To minimize the effect of nearby stromal cells in a neighborhood – which should not have active lineage-tracing – we did not allow this state to be 0, the uncut state. To maximize the alleles were used during spatial imputation, we required each state to be supported by at least 3 UMIs. We reported this procedure for each missing entry in the character matrix for a total of 5 iterations which continued to remove missing data from the character matrices with no apparent reduction in accuracy in simulations or held-out real data (**Figure S1J-N**).

Benchmarks of imputation and reconstruction accuracy

To benchmark the accuracy of spatial imputation and downstream effects on tree reconstruction, we utilized two different strategies:

- Synthetic data: First, we utilized the Cas9-based lineage-tracing simulation framework in Cassiopeia[41] (version 2.0.0, available at https://github.com/YosefLab/Cassiopeia). Specifically, we simulated trees using Cassiopeia's *BirthDeathSimulator* with the following parameters: 5000 extant cells, and utilized a LogNormal birth-waiting distribution parameterized by $\log(f)$ where *f* is a fitness coefficient that accumulates with each cell division (in each cell division, a new coefficient $f \sim N(0, 0.25)$ is drawn and added to the base fitness) and a standard deviation of 0.5. Then, we simulated lineage tracing data onto the tree with Cassiopeia's *Cas9LineageTracingDataSimulator* with desired mutation proportion of 0.7, 100 states, 39 cut sites (representing our system with approximately 13 intBCs, each with 3 cut-sites), and no missing data rates at this point. Then, we simulated spatial coordinates on each tree using the *ClonalSpatialDataSimulator* over a shape of (1,1,1) and sampled a 2D slice from this 3D simulation at random. Finally, we subsampled from this spatial array using the *UniformLeafSubsampler* in Cassiopeia with a rate of 0.4 (resulting in lineages with 2,000 observations) and induced random dropout at various rates: [0.1, 0.25, 0.5, 0.6, 0.7, 0.9]. We simulated 10 trees for each parameter combination.

As the spatial array simulated does not exactly match that from Slide-seq, we applied a modified *k-nearest-neighbor* graph construction approach, linking together spots to their closest 10 neighbors and performed spatial imputation (see section titled "Spatial imputation of lineage-tracing data"). We required concordance of 0.8 for the selected state and at least 5 votes. Since this simulated data does not include any normal cells, we do allow the imputation of the state 0. We reported the accuracy of this imputation strategy in **Figure S1J**). Then, we compared the tree reconstructing accuracies using the *triplets_correct* function in Cassiopeia for reconstructions with or without imputation and for different reconstruction strategies: modified Neighbor-Joining, Cassiopeia-Greedy, or a hybrid of these two approaches (see section "Phylogenetic reconstruction").

- Simulated held-out Slide-seq data: In the next experiment, we assessed the accuracy of recovering target-site data that was held-out from real Slide-seq data. To do this, for a given Slide-seq array, we masked out 10% of the observed data (supported by at least 3 UMIs) and performed spatial imputation in neighborhoods of 30μm using the strategy described previously (see section titled "Spatial imputation of lineage-tracing data). Similarly, we required a concordance of 0.8 and at least 5 votes in support of the imputed allele. We only considered samples where at least 10 states were imputed. Random predictions were obtained by shuffling the node labels in the neighborhood graph. We reported the average accuracy and total number of imputed values over five replicates in **Figure S1M**.

Simulation benchmarks of lineage-tracing pre-processing

As a feature of the Slide-seq is that multiple cells may be observed in one spot[57], multiple conflicting alleles can be observed for a given target site in a single spot. Typically, this would break the assumption of the Cassiopeia reconstruction pipeline (in single-cell approaches, we assume that only one allele can be tied to a given intBC and perform error correction or filtering otherwise). However, we implemented new reconstruction algorithms that can handle multiple conflicting states in each spot (see section entitled "Phylogenetic reconstruction") and simulated the effects of various pre-processing techniques.

First, we simulated trees on two-dimensional surfaces where various proportions of cells would be grouped together based on their spatial location. To do so, we simulated simple binary trees of 2000 cells and overlaid lineage-tracing data with Cassiopeia's *Cas9LineageTracingDataSimulator* function using the following parameters: 39 characters, a mutation proportion of 0.5, and no missing data. We then merged together cells using

Cassiopeia's *SupercellularSampler* method with rates of [0.1, 0.2, 0.3, 0.4, 0.5, 0.6]. We simulated 32 replicates.

For each replicate, we pre-processed character matrices according to three strategies. Here, the entry of the ith cell and j^{th} character (denoted as $\mathrm{X}[i,j]$) would contain a set of states $\mathrm{X}[i,j] = \{s_1, s_2, \dots, s_k\}$, each state occurring at some frequency $\mathrm{f}(s_i) = f_i$. In the first strategy ("collapse duplicates") we take the unique set of states so that $\mathrm{X}[i,j] = \{s_1, s_2, \dots, s_{k'}\}\ s.\mathrm{t.}\ f_i = 1\ \forall\ \mathrm{i} \in k'$; in the second strategy ("most common") we take the most common state, such that $\mathrm{X}[i,j] = argmax_{f(s')\ \forall s \in k} s'$; and the third strategy ("all states") we do not perform any filtering. In **Figure S1F** we report the tree reconstruction error (measured with normalized Robinson-Foulds distance) for trees reconstructed with Neighbor-Joining[63].

Phylogenetic reconstruction on Slide-seq data

To enable phylogenetic reconstruction on Slide-seq data in which multiple cells can be contained in a single spot and thus conflicting alleles are present, we implemented a Hybrid Cassiopeia-Greedy & Neighbor-Joining algorithm that could utilize conflicting allele states.

For Cassiopeia-Greedy, we modified the splitting decision rule to account for all states observed in a spot. Cassiopeia-Greedy is a simple, heuristic-based algorithm for reconstructing phylogenies that iteratively finds the most common state in a given population and splits samples into groups based on the presence or absence of the state. It is based on a perfect-phylogeny reconstruction algorithm[100] and has an efficient runtime of *O(mn)* for a population of *n* samples and *m* characters. Here, we changed the procedure to find the state with the highest frequency by allowing each sample to carry multiple states in a character. The runtime of this algorithm is still polynomial in the size of the sample population – *O(n(ms))* where in the worst case scenario every single state is observed in every single character; given the size of the spatial array, this is exceedingly uncommon and typically 1-3 cells are captured per spot[57].

For Neighbor-Joining, we utilized the standard algorithm[63] but with a modified distance map that accounts for multiple states per spot. Specifically, we implemented a new dissimilarity metric that takes in two sets of states S_1 and S_2 and computes all the pairwise allelic dissimilarities and reports a linkage similar to hierarchical clustering. Here, we use the modified allelic dissimilarity for two states s_i, s_j to compute distances between pairs of states, previously described[41,47,50]:

$$h'^{(s_i,s_j)} = \begin{cases} 2 \;\; if \; s_i \neq s_j \neq 0 \\ 1 \;\; if \; s_i \neq s_j \;\; and \; (s_i = 0 \; or \; s_j = 0) \\ 0 \;\; otherwise \end{cases}$$

In the case where weights are passed in, then the dissimilarity function is computed as follows:

$$h'^{(s_i,s_j)} = \begin{cases} \mathrm{w_i} w_j \;\; if \; s_i \neq s_j \neq 0 \\ w_i \;\; if \; s_i \neq s_j \;\; and \; s_j = 0 \\ w_j \; if \; s_i \neq s_j \; and \; s_i = 0 \\ 0 \;\; otherwise \end{cases}$$

Then, we utilized a single linkage function such that only the smallest modified allelic dissimilarity across all pairs of states in S_1 and S_2 was used. This is to maintain such that if the same state is observed in two spots, the dissimilarity returned is 0.

For the hybrid reconstruction, we utilized the modified Cassiopeia-Greedy algorithm described above until subpopulations of size 1000 cells were found, at which point Neighbor-Joining with the modified dissimilarity metric was used to resolve phylogenetic relationships. We utilized state probabilities inferred from all Slide-seq and Slide-tags datasets and used the weight $-\log(p_i)$ for state s_i during tree reconstruction.

Phylogenetic reconstruction on Slide-tags data

We utilized the standard Cassiopeia-Hybrid[41] algorithm for reconstructing Slide-tags phylogenies. Briefly, this approach applies the heuristic-based Cassiopeia-Greedy algorithm to reconstruct relationships between the major subclones and then applies the maximum-parsimony-based Cassiopeia-ILP algorithm to solve fine-grained phylogenetic structure in smaller populations. As previously described in detail[41], Cassiopeia-ILP proceeds by building a potential graph of all possible ancestral states (constrained in size by a user-defined parameter) and solves for the maximum-parsimony phylogeny by reconstructing a Steiner Tree on this data structure. The Steiner Tree problem is solved via an Integer Linear Program (ILP) allowed a certain time to converge. Here, the transition between Cassiopeia-Greedy and -ILP algorithms is determined by the distance to the latest common ancestor (LCA) of a subpopulation.

We applied the Cassiopeia-Hybrid algorithm with state priors inferred from all samples[41,47,50], determined the switch between Greedy and ILP algorithms using an LCA cutoff of 20, devised a potential graph of 10000 nodes with a maximum distance of 15 across nodes (maximum_potential_graph_lca_distance=15), and allowed the ILP 12600s to converge.

Slide-tags cell type annotation

1010 After performing quality-control on Slide-tags gene expression data, we assigned cell
1011 types first by integrating Slide-tags data with an annotated single-cell gene expression reference
1012 dataset of KP-Tracer tumors[50] with scANVI[101]. To do so, first identified 4,750 variable genes using
1013 Scanpy's[97] *highly_variable_genes* function using the *flavor="seurat_v3"* and raw counts. We then
1014 trained an scVI model[102,103] on the joint dataset and these variable genes using 3 layers and 70
1015 latent dimensions over 1000 epochs. Then, we transferred labels from the single-cell reference
1016 dataset to the Slide-tags nuclei with scANVI utilizing 200 samples per label and 100 epochs.
1017 Through this, we used the *gene_likelihood="nb"* setting in training models and used the
1018 technology – Slide-tags or single-cell – variable to signify batch.
1019 After training this model, subset to the scANVI embeddings to the Slide-tags data only and
1020 re-clustered the data with Scanpy[97] using the Leiden algorithm[104] and resolution 1.2. We then split
1021 clusters into those that appeared to derive from tumor/epithelial cells or those that derived from
1022 the stroma. To call tumor or epithelial clusters, we evaluated if a cluster had an abundance of
1023 tumor nuclei (defined as nuclei with target site data and at least 20% of their sites containing
1024 indels) or expressed the epithelial-lineage marker *Nxk2-1*. Immune cell clusters were identified
1025 based on the marker *Cd45 (Ptprc)* and other stromal cells were identified by expression of *Pdgfra,*
1026 *Col1a1,* or *Col5a1* (fibroblasts) or *Pecam1* (endothelial cells). For each subsetted dataset
1027 (tumor/epithelia or stromal), we reclustered the data and annotated cell types based on
1028 annotations predicted with scANVI and differentially expressed genes identified with Scanpy's
1029 *rank_genes_group* function (using the Wilcoxon test).
1030
1031 **Assessment of Slide-tags tumor cell type signatures in previous KP-Tracer data**
1032 To test the portability and accuracy of the tumor clusters identified in Slide-tags, we
1033 assessed the activity of gene signatures in the previous KP-Tracer data[50]. Specifically, we for
1034 each cell-type identified in Slide-tags, we computed the top 100 differentially-expressed genes
1035 using the Wilcoxon test in Scanpy[97] and further filtered genes to have a log-fold change > 1 and
1036 an FDR-corrected p-value <= 0.01, and an AUROC of at least 0.6. We then used these genes to
1037 define a transcriptional signature for each Slide-tags cell type. each of these signatures, we
1038 scored the activity in cell types identified in Slide-tags data and the previous KP-Tracer dataset
1039 using the *score_genes* function using *n_bins=30* and *ctrl_size* equal to the number of genes in
1040 the gene set. Signatures were computed on scaled, log-normalized counts. The result of this
1041 analysis is presented in **Figure S2B**.
1042
1043 **Slide-seq spatial community detection and scoring**

To identify spatial communities in Slide-seq data, first applied the Hotspot[105] algorithm for detecting spatially autocorrelated gene sets on each sample. In the spatial mode, this algorithm constructs a nearest neighbor graph based on spatial coordinates, computes an autocorrelation statistic for each gene, and then identifies modules of genes that have significant pairwise autocorrelation values. Here, we applied Hotspot with 20 neighbors, and FDR threshold of 0.01 to identify spatially autocorrelated genes, and a minimum module size of 50 genes.

Then, to identify robust modules of genes that appear across tumors, we assessed the Jaccard overlap between all pairs of modules across all tumors and filtered out modules that did not have a Jaccard overlap of at least 0.2 with at most one other module. We then performed Z-normalization on these Jaccard statistics and clustered these using hierarchical clustering (using the “ward” method on Euclidean distances) and identified 11 clusters, representing robust spatial modules.

As these robust modules are collections of modules across all samples we analyzed, we distilled these down to a set of genes – representing what we call a “spatial community” in this study – by taking genes that appear in at least 25% of the modules in the robust module. Using these genes in the spatial community, we compute the activity of these communities for each spot (termed “community scores”) using the *score_genes* function in Scanpy[97] with *ctrl_size=100* and *n_bins=30.* We computed these scores on scaled, log-normalized gene expression counts. To obtain community assignments for each spot, we took the community with the highest score.

Tumor segmentation

To segment tumors, we utilized the SpatialData[106] package and the napari-spatialdata viewer for interactive annotation. To identify tumor areas on a sample, we overlaid phylogenetic subclones and the number of target-site UMIs detected and manually segmented areas that appeared to be (a) phylogenetically related and (b) had elevated target-site UMIs indicative of tumor regions. We saved these annotations and used the segmentations to perform downstream analysis on a tumor-by-tumor basis.

Fitness signature calculation

To quantify fitness signature scores, we utilized a gene set that was found to be associated with changes in fitness from our previous single-cell KP-Tracer study[50]. Using this gene set, we quantified the transcriptional activity for each spot in Slide-seq data by applying the *score_genes* function in Scanpy[97] with *ctrl_size=100* and *n_bins=30.* We computed these scores on scaled, log-normalized gene expression counts.

Phylogenetic fitness inference

We quantified fitness on Slide-seq and Slide-tags phylogenies by utilizing the *LBIFitness* fitness estimator in Cassiopeia[41]. This function wraps a fitness estimator based on the "local branching index" as previously described[107]. This procedure has been previously used in our system[50]. Primed by the true single-cell resolution of Slide-tags trees, we estimated branch lengths using the *IIDExponentialMLE* branch length estimator in Cassiopeia. This function implements a function that provides maximum-likelihood branch lengths on a tree topology given the pattern of edits observed in the leaves and an assumptions about the irreversibility of Cas9 editing[108]. Using the branch lengths determined by this maximum-likelihood procedure, we estimated single-cell fitness on Slide-tags trees.

Due to the increased missingness on Slide-seq trees and the fact that MLE-based branch length approaches have not been benchmarked on Slide-seq data, we performed a more conservative branch length estimation, as done previously[50]. Here, branches had a length of 1 if they had any mutations along them, otherwise they had a branch length of 0. Using these branch lengths, we estimated single-cell fitness on Slide-seq trees.

Single-cell clonal plasticity quantification

To estimate single-cell clonal plasticity on phylogenies, we applied approaches described in our previous studies[50,69]. Specifically, on Slide-tags data where we have true single-cell data and associated cell type identities, we applied the *score_small_parsimony* procedure to all nodes in a tree using *meta_item="cell_type"* and normalized by the number of leaves in the subtree induced by the node. Then, we computed plasticity for each cell by averaging together all the normalized parsimonies.

Since we do not have true single-cell resolution for Slide-seq data, we employed the L2 plasticity score described in our previous study[50], using community scores. Specifically, let C_i be the vector of community scores associated with spot i. For this spot i we found its closest phylogenetic neighbors (denoted by set *N*) and then computed the L2-Plasticity ($L2_p(i)$) for this spot by the average Euclidean distance to the vector of community scores for these neighbors:

$$L2_P(i) = \frac{1}{|N|}\sum_{k \in N} \left|\left|C_i - C_k\right|\right|_2$$

All scores were unit scaled.

1111 **Differential expression and abundance in neighborhoods of high-fitness cells**

1112 To identify changes in gene expression and spatial communities associated with fitness,
1113 we first stratified cells into high- and low-fitness groups. In Slide-seq data, we computed single-
1114 cell fitness scores (see section above entitled "Phylogenetic fitness inference") and identified a
1115 threshold separating two modes using *scipy.signal.argrelmin* in the merged fitness distributions
1116 and split spots into high-fitness groups and low-fitness groups based on this threshold. Only
1117 tumors with at least 200 observations with lineage-tracing data were used. As each fitness
1118 distribution is normalized within individual tumors to be unit-scaled, this approach finds a global
1119 pattern in high- and low-fitness cells. Then, we constructed a neighborhood graph connecting
1120 each spot to all other spots within 30μm. The community scores for all communities were
1121 computed in these neighborhoods and the distributions in neighborhoods of high- and low-fitness
1122 cell were reported in **Figure S3L.**

1123 In Slide-tags data, high and low-fitness cells were similarly determined from the
1124 distribution of all fitnesses using *scipy.signal.argmin*. As Slide-tags is sparser than Slide-seq, we
1125 constructed neighborhoods using the closest 20 cells (an example is shown in **Figure S3K**). We
1126 then identified the differentially-expressed genes in neighborhoods of high- and low-fitness cells
1127 of all Macrophage and Fibroblast subsets using the t-test as implemented in Scanpy's[97]
1128 *rank_genes_groups* function. For the Macrophage analysis, we evaluated the Alveolar
1129 Macrophages, *Arg1*+ TAMs, *Pecam1*+ TAMs, and *Vegfa*+ TAMs; for the Fibroblast analysis we
1130 evaluated the *Wt1*+ fibroblast, iCAF-like and myCAF-like populations. Genes expressed in fewer
1131 than 50 cells were filtered out, and the differential expression statistics for the top 10,000 genes
1132 were computed. Genes with an absolute log2-fold-change > 1 and an FDR-corrected p-value <
1133 0.01 were marked as significantly differentially expressed. To compute enrichments in these
1134 neighborhoods, we computed the frequency of cell types in neighborhoods of high- and low-
1135 fitness cells and divided by the expected fraction of these cell types given the overall distribution
1136 and size of the Slide-tags array.

1137 GO Term analysis of differentially-expressed genes was performed using gseapy[109]
1138 (version 1.1.3) with the following gene sets: "WikiPathways_2019_Mouse", "Reactome_2022",
1139 "GO_Biological_Process_2023", "GO_Molecular_Function_2023", and "KEGG_2019_Mouse".
1140 Significant terms are reported in **Supplementary Table 2**.

1141

1142 **Differential expression in neighborhoods of high-plasticity cells in Slide-seq**

1143 Similar to the fitness-based analysis (see section entitled "Differential expression in
1144 neighborhoods of high-fitness cells"), we stratified cells into high- and low-plasticity groups. After

quantifying the L2-clonal plasticity score in Slide-seq data, we determined a threshold separating high- and low-plasticity regions if a cell had greater plasticity than the 60th percentile or less than the 40th percentile, respectively. Then, we constructed a neighborhood graph connecting each spot to all other spots within 30μm. The community scores for all communities were computed in these neighborhoods and the distributions in neighborhoods of high- and low-plasticity cells were reported in **Figure S3M.**

Coarse-grained alignment of Slide-seq data

To track the three-dimensional structure of clones across sampled layers in **Figure 4**, we utilized the non-imputed processed target-site data (see section entitled "Slide-seq lineage tracing target-site data processing"). To maximize fidelity of slide registration, we enforced hard quality-control cutoffs, requiring each spot be supported by at least 7 UMIs and then subsequently each intBC-allele to be supported by at least 5 UMIs. We filtered out spots that had less than 20% of their sites reporting indels, or more than 70% missing data. We then computed modified allelic distances (see section above entitled "Phylogenetic reconstruction on Slide-seq data") between all pairs of spots across layers. Modified allelic distances here are normalized by the number characters shared between two spots (thus are normalized to values between 0-2). For computational reasons, we did not allow ambiguous alleles (taking only the most frequent allele per intBC in a spot) as the distance calculation is memory- and time-intensive. Using this distance matrix, we computed allelic evolutionary couplings using *compute_evolutionary_coupling* function in Cassiopeia with the following parameters: *minimum_proportion = 0.0002, number_of_shuffles = 100*. We then normalized the evolutionary coupling as previously described[50], as so:

$$\tilde{E}(i,j) = e^{\frac{-E(i,j)}{\max(E[i',j'])}}$$

Where *E(i,j)* denotes the allelic evolutionary coupling between spot *i* and *j* and *max(E[i', j'])* indicates the maximum value across all evolutionary couplings. Clusters identified via hierarchical clustering of the normalized allelic evolutionary coupling matrix were used as registered Tumor IDs in **Figure 4B**.

Detection of metastasis-initiating subclones

To detect metastasis-initiating subclones in primary tumors, we created a shared character matrix between all lung sections profiled with 1cm x 1cm Curio arrays and Slide-seq samples of

1178 metastases. We filtered out spots that did not have at least 2 UMIs intBC-alleles that were not
1179 supported by at least 2 UMIs. We further filtered out spots that had fewer than 20% of their target-
1180 sites cut and more than 70% missingness. For computational reasons, we did not allow
1181 ambiguous alleles (taking only the most frequent allele per intBC in a spot) as the distance
1182 calculation is memory- and time-intensive. We then computed a shared metastatic parental allele
1183 state by taking states that were shared amongst 60% of spots in metastases profiled with Slide-
1184 seq. From this parental state, we computed the modified allelic distance (normalized by the
1185 number of shared characters) to all spots in the lung sample. We performed a similar analysis in
1186 paired Slide-tags data, computing the normalized modified allelic distances from all nuclei to the
1187 metastatic parental allele state.
1188
1189 **Differential expression across metastatic cascade**
1190 We identified gene expression changes across niches associated with the metastatic
1191 cascade by employing the distances computed in the section above entitled "Detection of
1192 metastasis-initiating subclones". We identified the metastasis-originating subclone as localizing
1193 to T2, so T1, T3 and T4 were determined to be Primary tumors without any relationship to the
1194 metastases. Focusing on T2, we further segmented it into a metastasis-initiating subclone (T2-
1195 Met) and other subclones (T2-NonMet). Specifically, we assigned cells to a metastatic subclone
1196 if their normalized modified allelic distance was less than 0.8. Then, using these assignments, we
1197 performed watershed segmentation with a custom procedure. Specifically, we binned signal into
1198 bins of 100 adjacent spots, applied a Gaussian filter with a sigma of 1.5 (with the Python package
1199 *skimage*) and then applied an Otsu threshold and dilation. We then applied an exact distance
1200 transform with *scipy.ndimage.distance_transform_edt* and computed a Watershed mask over
1201 peaks identified with *skimage.feature.peak_local_max* with a goal of identifying one tumor. This
1202 segmented subclone was labeled as T2-Met, and the remainder of the tumor was called T2-
1203 NonMet. We then performed differential expression across the library-size-normalized, logged
1204 counts of four groups (Primary tumors without metastatic relationship; T2-Met; T2-NonMet; and
1205 metastases) using a t-test implemented in Scanpy's[97] *rank_genes_groups* and reported the log2-
1206 fold-change in **Figure 4G.**
1207 Signature scores for TGFβ signaling were computed using MSigDB's
1208 "HALLMARK_TGF_BETA_SIGNALING" signature. Signature scores for collagen were computed
1209 for a custom gene set consisting of *Acta2, Col1a1, Col2a1, Col3a1, Col5a1,* and *Col12a1*.
1210 Significance was computed using a one-sided *t*-test assessing if signature scores were higher in
1211 the metastatic tumor as compared to the primary tumor.

1212 **Differential cell type abundance in metastatic neighborhoods**

1213 Similar to analyses stratifying Slide-tags cells into neighborhoods of high- and low-fitness
1214 cells, we stratified cells into neighborhoods of cells closely related to metastases. As with
1215 determining cells related to metastases in Slide-seq data, we computed the distance to the
1216 parental metastatic allele and assigned cells with distances smaller than 0.8 as related to
1217 metastases. Then, we reconstructed spatial neighborhoods of the closest 20 cells and quantified
1218 cell type enrichments based on the frequencies of cell types in these neighborhoods and the
1219 overall frequency in a Slide-tags array.

1220

1221 **REFERENCES**

1222 1. Nowell, P. C. The clonal evolution of tumor cell populations. *Science* **194**, 23–28 (1976).
1223 2. Vogelstein, B. *et al.* Cancer genome landscapes. *Science* **339**, 1546–1558 (2013).
1224 3. Binnewies, M. *et al.* Understanding the tumor immune microenvironment (TIME) for effective
1225 therapy. *Nat. Med.* **24**, 541–550 (2018).
1226 4. de Visser, K. E. & Joyce, J. A. The evolving tumor microenvironment: From cancer initiation
1227 to metastatic outgrowth. *Cancer Cell* **41**, 374–403 (2023).
1228 5. Northey, J. J., Przybyla, L. & Weaver, V. M. Tissue force programs cell fate and tumor
1229 aggression. *Cancer Discov.* **7**, 1224–1237 (2017).
1230 6. Noble, R. *et al.* Spatial structure governs the mode of tumour evolution. *Nat. Ecol. Evol.* **6**,
1231 207–217 (2021).
1232 7. Derynck, R., Turley, S. J. & Akhurst, R. J. TGFβ biology in cancer progression and
1233 immunotherapy. *Nat. Rev. Clin. Oncol.* **18**, 9–34 (2021).
1234 8. Fang, J. S., Gillies, R. D. & Gatenby, R. A. Adaptation to hypoxia and acidosis in
1235 carcinogenesis and tumor progression. *Semin. Cancer Biol.* **18**, 330–337 (2008).
1236 9. Carmona-Fontaine, C. *et al.* Emergence of spatial structure in the tumor microenvironment
1237 due to the Warburg effect. *Proc. Natl. Acad. Sci. U. S. A.* **110**, 19402–19407 (2013).
1238 10. Houlahan, K. E. *et al.* Germline-mediated immunoediting sculpts breast cancer subtypes and
1239 metastatic proclivity. *Science* **384**, (2024).
1240 11. McAllister, S. S. & Weinberg, R. A. The tumour-induced systemic environment as a critical
1241 regulator of cancer progression and metastasis. *Nat. Cell Biol.* **16**, 717–727 (2014).
1242 12. Schwartz, R. & Schäffer, A. A. The evolution of tumour phylogenetics: principles and practice.
1243 *Nat. Rev. Genet.* **18**, 213–229 (2017).

13. Jones, M. G., Yang, D. & Weissman, J. S. New tools for lineage tracing in cancer in vivo. *Annu. Rev. Cancer Biol.* **7**, (2023).

14. McGranahan, N. & Swanton, C. Clonal Heterogeneity and Tumor Evolution: Past, Present, and the Future. *Cell* **168**, 613–628 (2017).

15. Davis, A., Gao, R. & Navin, N. Tumor evolution: Linear, branching, neutral or punctuated? *Biochim. Biophys. Acta Rev. Cancer* **1867**, 151–161 (2017).

16. Hu, Z. & Curtis, C. Inferring tumor phylogenies from multi-region sequencing. *Cell Syst.* **3**, 12–14 (2016).

17. Jones, S. *et al.* Comparative lesion sequencing provides insights into tumor evolution. *Proc. Natl. Acad. Sci. U. S. A.* **105**, 4283–4288 (2008).

18. Gerlinger, M. *et al.* Intratumor heterogeneity and branched evolution revealed by multiregion sequencing. *N. Engl. J. Med.* **366**, 883–892 (2012).

19. Jamal-Hanjani, M. *et al.* Tracking the evolution of non–small-cell lung cancer. *N. Engl. J. Med.* **376**, 2109–2121 (2017).

20. Schwarz, R. F. *et al.* Spatial and temporal heterogeneity in high-grade serous ovarian cancer: A phylogenetic analysis. *PLoS Med.* **12**, e1001789 (2015).

21. Sottoriva, A. *et al.* A Big Bang model of human colorectal tumor growth. *Nat. Genet.* **47**, 209–216 (2015).

22. Zhao, Y. *et al.* Selection of metastasis competent subclones in the tumour interior. *Nat. Ecol. Evol.* **5**, 1033–1045 (2021).

23. Turajlic, S. *et al.* Tracking cancer evolution reveals constrained routes to metastases: TRACERx renal. *Cell* **173**, 581-594.e12 (2018).

24. Navin, N. *et al.* Tumour evolution inferred by single-cell sequencing. *Nature* **472**, 90–94 (2011).

25. Zhao, T. *et al.* Spatial genomics enables multi-modal study of clonal heterogeneity in tissues. *Nature* **601**, 85–91 (2022).

26. Erickson, A. *et al.* Spatially resolved clonal copy number alterations in benign and malignant tissue. *Nature* **608**, 360–367 (2022).

27. Lomakin, A. *et al.* Spatial genomics maps the structure, nature and evolution of cancer clones. *Nature* **611**, 594–602 (2022).

28. Househam, J. *et al.* Phenotypic plasticity and genetic control in colorectal cancer evolution. *Nature* **611**, 744–753 (2022).

29. Heiser, C. N. *et al.* Molecular cartography uncovers evolutionary and microenvironmental dynamics in sporadic colorectal tumors. *Cell* **186**, 5620-5637.e16 (2023).

30. Frieda, K. L. *et al.* Synthetic recording and in situ readout of lineage information in single cells. *Nature* **541**, 107–111 (2017).

31. Chow, K.-H. K. *et al.* Imaging cell lineage with a synthetic digital recording system. *Science* **372**, (2021).

32. Chan, M. M. *et al.* Molecular recording of mammalian embryogenesis. *Nature* **570**, 77–82 (2019).

33. McKenna, A. *et al.* Whole-organism lineage tracing by combinatorial and cumulative genome editing. *Science* **353**, aaf7907 (2016).

34. Spanjaard, B. *et al.* Simultaneous lineage tracing and cell-type identification using CRISPR–Cas9-induced genetic scars. *Nat. Biotechnol.* **36**, 469–473 (2018).

35. He, Z. *et al.* Lineage recording in human cerebral organoids. *Nat. Methods* **19**, 90–99 (2022).

36. Choi, J. *et al.* A time-resolved, multi-symbol molecular recorder via sequential genome editing. *Nature* **608**, 98–107 (2022).

37. Hwang, B. *et al.* Lineage tracing using a Cas9-deaminase barcoding system targeting endogenous L1 elements. *Nat. Commun.* **10**, 1–9 (2019).

38. Alemany, A., Florescu, M., Baron, C. S., Peterson-Maduro, J. & van Oudenaarden, A. Whole-organism clone tracing using single-cell sequencing. *Nature* **556**, 108–112 (2018).

39. Kalhor, R., Mali, P. & Church, G. M. Rapidly evolving homing CRISPR barcodes. *Nat. Methods* **14**, 195–200 (2017).

40. Li, L. *et al.* A mouse model with high clonal barcode diversity for joint lineage, transcriptomic, and epigenomic profiling in single cells. *Cell* **186**, 5183-5199.e22 (2023).

41. Jones, M. G. *et al.* Inference of single-cell phylogenies from lineage tracing data using Cassiopeia. *Genome Biol.* **21**, 92 (2020).

42. Sashittal, P., Schmidt, H., Chan, M. & Raphael, B. J. Startle: A star homoplasy approach for CRISPR-Cas9 lineage tracing. *Cell Syst.* **14**, 1113-1121.e9 (2023).

43. Fang, W. *et al.* Quantitative fate mapping: A general framework for analyzing progenitor state dynamics via retrospective lineage barcoding. *Cell* **185**, 4604-4620.e32 (2022).

44. Gong, W. *et al.* Benchmarked approaches for reconstruction of in vitro cell lineages and in silico models of C. elegans and M. musculus developmental trees. *Cell Syst* **12**, 810-826.e4 (2021).

45. Pan, X., Li, H., Putta, P. & Zhang, X. LinRace: cell division history reconstruction of single cells using paired lineage barcode and gene expression data. *Nat. Commun.* **14**, 1–15 (2023).

46. Schiffman, J. S. *et al.* Defining heritability, plasticity, and transition dynamics of cellular phenotypes in somatic evolution. *Nat. Genet.* 1–11 (2024).

1312 47. Quinn, J. J. *et al.* Single-cell lineages reveal the rates, routes, and drivers of metastasis in
1313 cancer xenografts. *Science* **371**, (2021).
1314 48. Simeonov, K. P. *et al.* Single-cell lineage tracing of metastatic cancer reveals selection of
1315 hybrid EMT states. *Cancer Cell* (2021) doi:10.1016/j.ccell.2021.05.005.
1316 49. Zhang, W. *et al.* The bone microenvironment invigorates metastatic seeds for further
1317 dissemination. *Cell* **184**, 2471-2486.e20 (2021).
1318 50. Yang, D. *et al.* Lineage tracing reveals the phylodynamics, plasticity, and paths of tumor
1319 evolution. *Cell* (2022) doi:10.1016/j.cell.2022.04.015.
1320 51. Jackson, E. L. *et al.* Analysis of lung tumor initiation and progression using conditional
1321 expression of oncogenic K-ras. *Genes Dev.* **15**, 3243–3248 (2001).
1322 52. Jackson, E. L. *et al.* The differential effects of mutant p53 alleles on advanced murine lung
1323 cancer. *Cancer Res.* **65**, 10280–10288 (2005).
1324 53. Winslow, M. M. *et al.* Suppression of lung adenocarcinoma progression by Nkx2-1. *Nature*
1325 **473**, 101–104 (2011).
1326 54. LaFave, L. M. *et al.* Epigenomic State Transitions Characterize Tumor Progression in Mouse
1327 Lung Adenocarcinoma. *Cancer Cell* **38**, 212-228.e13 (2020).
1328 55. Marjanovic, N. D. *et al.* Emergence of a High-Plasticity Cell State during Lung Cancer
1329 Evolution. *Cancer Cell* **38**, 229-246.e13 (2020).
1330 56. Stickels, R. R. *et al.* Highly sensitive spatial transcriptomics at near-cellular resolution with
1331 Slide-seqV2. *Nat. Biotechnol.* **39**, 313–319 (2021).
1332 57. Rodriques, S. G. *et al.* Slide-seq: A scalable technology for measuring genome-wide
1333 expression at high spatial resolution. *Science* **363**, 1463–1467 (2019).
1334 58. Russell, A. J. C. *et al.* Slide-tags enables single-nucleus barcoding for multimodal spatial
1335 genomics. *Nature* **625**, 101–109 (2024).
1336 59. Ståhl, P. L. *et al.* Visualization and analysis of gene expression in tissue sections by spatial
1337 transcriptomics. *Science* **353**, 78–82 (2016).
1338 60. Liu, Y. *et al.* High-spatial-resolution multi-omics sequencing via deterministic barcoding in
1339 tissue. *Cell* **183**, 1665-1681.e18 (2020).
1340 61. Sutherland, K. D. *et al.* Multiple cells-of-origin of mutant K-Ras-induced mouse lung
1341 adenocarcinoma. *Proc. Natl. Acad. Sci. U. S. A.* **111**, 4952–4957 (2014).
1342 62. Arlauckas, S. P. *et al.* Arg1 expression defines immunosuppressive subsets of tumor-
1343 associated macrophages. *Theranostics* **8**, 5842–5854 (2018).
1344 63. Saitou, N. & Nei, M. The neighbor-joining method: a new method for reconstructing
1345 phylogenetic trees. *Mol. Biol. Evol.* **4**, 406–425 (1987).

1346 64. You, Y. *et al.* Systematic comparison of sequencing-based spatial transcriptomic methods.
1347 *Nat. Methods* (2024) doi:10.1038/s41592-024-02325-3.
1348 65. Chuang, C.-H. *et al.* Molecular definition of a metastatic lung cancer state reveals a targetable
1349 CD109-Janus kinase-Stat axis. *Nat. Med.* **23**, 291–300 (2017).
1350 66. Lee, J. Y. *et al.* Senescent fibroblasts in the tumor stroma rewire lung cancer metabolism and
1351 plasticity. *bioRxivorg* (2024) doi:10.1101/2024.07.29.605645.
1352 67. Bill, R. *et al.* CXCL9:SPP1 macrophage polarity identifies a network of cellular programs that
1353 control human cancers. *Science* **381**, 515–524 (2023).
1354 68. Lewinsohn, M. A., Bedford, T., Müller, N. F. & Feder, A. F. State-dependent evolutionary
1355 models reveal modes of solid tumour growth. *Nat. Ecol. Evol.* **7**, 581–596 (2023).
1356 69. Jones, M. G., Rosen, Y. & Yosef, N. Interactive, integrated analysis of single-cell
1357 transcriptomic and phylogenetic data with PhyloVision. *Cell Rep Methods* **2**, 100200 (2022).
1358 70. Moran, P. A. P. Notes on continuous stochastic phenomena. *Biometrika* **37**, 17–23 (1950).
1359 71. Hayashi, M. *et al.* Induction of glucose transporter 1 expression through hypoxia-inducible
1360 factor 1alpha under hypoxic conditions in trophoblast-derived cells. *J. Endocrinol.* **183**, 145–154
1361 (2004).
1362 72. Zhang, J. Z., Behrooz, A. & Ismail-Beigi, F. Regulation of glucose transport by hypoxia. *Am.*
1363 *J. Kidney Dis.* **34**, 189–202 (1999).
1364 73. Quail, D. F. & Joyce, J. A. Microenvironmental regulation of tumor progression and
1365 metastasis. *Nat. Med.* **19**, 1423–1437 (2013).
1366 74. Lee, J. H. *et al.* TGF-β and RAS jointly unmask primed enhancers to drive metastasis. *Cell*
1367 (2024) doi:10.1016/j.cell.2024.08.014.
1368 75. McGinnis, C. S. *et al.* The temporal progression of lung immune remodeling during breast
1369 cancer metastasis. *Cancer Cell* **42**, 1018-1031.e6 (2024).
1370 76. Gong, Z. *et al.* Lung fibroblasts facilitate pre-metastatic niche formation by remodeling the
1371 local immune microenvironment. *Immunity* **55**, 1483-1500.e9 (2022).
1372 77. Kaczanowska, S. *et al.* Genetically engineered myeloid cells rebalance the core immune
1373 suppression program in metastasis. *Cell* **184**, 2033-2052.e21 (2021).
1374 78. Murdoch, C., Muthana, M. & Lewis, C. E. Hypoxia regulates macrophage functions in
1375 inflammation. *J. Immunol.* **175**, 6257–6263 (2005).
1376 79. Kugeratski, F. G. *et al.* Hypoxic cancer-associated fibroblasts increase NCBP2-AS2/HIAR to
1377 promote endothelial sprouting through enhanced VEGF signaling. *Sci. Signal.* **12**, eaan8247
1378 (2019).

80. Corzo, C. A. *et al.* HIF-1α regulates function and differentiation of myeloid-derived suppressor cells in the tumor microenvironment. *J. Exp. Med.* **207**, 2439–2453 (2010).
81. Korbecki, J. *et al.* Hypoxia alters the expression of CC chemokines and CC chemokine receptors in a tumor-A literature review. *Int. J. Mol. Sci.* **21**, 5647 (2020).
82. Chaturvedi, P., Gilkes, D. M., Takano, N. & Semenza, G. L. Hypoxia-inducible factor-dependent signaling between triple-negative breast cancer cells and mesenchymal stem cells promotes macrophage recruitment. *Proc. Natl. Acad. Sci. U. S. A.* **111**, E2120-9 (2014).
83. França, G. S. *et al.* Cellular adaptation to cancer therapy along a resistance continuum. *Nature* **631**, 876–883 (2024).
84. Becker, W. R. *et al.* Single-cell analyses define a continuum of cell state and composition changes in the malignant transformation of polyps to colorectal cancer. *Nat. Genet.* **54**, 985–995 (2022).
85. Hanahan, D. Hallmarks of cancer: New dimensions. *Cancer Discov.* **12**, 31–46 (2022).
86. Kakani, P. *et al.* Hypoxia-induced CTCF promotes EMT in breast cancer. *Cell Rep.* **43**, 114367 (2024).
87. Zhang, L. *et al.* Hypoxia induces epithelial-mesenchymal transition via activation of SNAI1 by hypoxia-inducible factor -1α in hepatocellular carcinoma. *BMC Cancer* **13**, 108 (2013).
88. Rankin, E. B. & Giaccia, A. J. Hypoxic control of metastasis. *Science* **352**, 175–180 (2016).
89. Zhao, W. *et al.* A cellular and spatial atlas of TP53 -associated tissue remodeling in lung adenocarcinoma. *bioRxivorg* (2024) doi:10.1101/2023.06.28.546977.
90. De Zuani, M. *et al.* Single-cell and spatial transcriptomics analysis of non-small cell lung cancer. *Nat. Commun.* **15**, 4388 (2024).
91. Enfield, K. S. S. *et al.* Spatial architecture of myeloid and T cells orchestrates immune evasion and clinical outcome in lung cancer. *Cancer Discov.* **14**, 1018–1047 (2024).
92. Greenwald, A. C. *et al.* Integrative spatial analysis reveals a multi-layered organization of glioblastoma. *Cell* **187**, 2485-2501.e26 (2024).
93. Chen, W. *et al.* Symbolic recording of signalling and cis-regulatory element activity to DNA. *Nature* **632**, 1073–1081 (2024).
94. Kempton, H. R., Love, K. S., Guo, L. Y. & Qi, L. S. Scalable biological signal recording in mammalian cells using Cas12a base editors. *Nat. Chem. Biol.* **18**, 742–750 (2022).
95. Melsted, P. *et al.* Modular, efficient and constant-memory single-cell RNA-seq preprocessing. *Nat. Biotechnol.* **39**, 813–818 (2021).
96. Fleming, S. J. *et al.* Unsupervised removal of systematic background noise from droplet-based single-cell experiments using CellBender. *Nat. Methods* **20**, 1323–1335 (2023).

97. Wolf, F. A., Angerer, P. & Theis, F. J. SCANPY: large-scale single-cell gene expression data analysis. *Genome Biol.* **19**, 15 (2018).
98. Martin, M. Cutadapt removes adapter sequences from high-throughput sequencing reads. *EMBnet J.* **17**, 10 (2011).
99. *Density-Based Algorithm for Discovering Clusters in Large Spatial Databases with Noise*.
100. Gusfield, D. Efficient algorithms for inferring evolutionary trees. *Networks (N. Y.)* **21**, 19–28 (1991).
101. Xu, C. *et al.* Probabilistic harmonization and annotation of single-cell transcriptomics data with deep generative models. *Mol. Syst. Biol.* **17**, e9620 (2021).
102. Lopez, R., Regier, J., Cole, M. B., Jordan, M. I. & Yosef, N. Deep generative modeling for single-cell transcriptomics. *Nat. Methods* **15**, 1053–1058 (2018).
103. Gayoso, A. *et al.* scvi-tools: a library for deep probabilistic analysis of single-cell omics data. *bioRxiv* 2021.04.28.441833 (2021) doi:10.1101/2021.04.28.441833.
104. Traag, V. A., Waltman, L. & van Eck, N. J. From Louvain to Leiden: guaranteeing well-connected communities. *Sci. Rep.* **9**, 5233 (2019).
105. DeTomaso, D. & Yosef, N. Hotspot identifies informative gene modules across modalities of single-cell genomics. *Cell Syst* **12**, 446-456.e9 (2021).
106. Marconato, L. *et al.* SpatialData: an open and universal data framework for spatial omics. *Nat. Methods* 1–5 (2024).
107. Neher, R. A., Russell, C. A. & Shraiman, B. I. Predicting evolution from the shape of genealogical trees. *Elife* **3**, (2014).
108. Prillo, S., Ravoor, A., Yosef, N. & Song, Y. S. ConvexML: Scalable and accurate inference of single-cell chronograms from CRISPR/Cas9 lineage tracing data. *bioRxivorg* (2023) doi:10.1101/2023.12.03.569785.
109. Fang, Z., Liu, X. & Peltz, G. GSEApy: a comprehensive package for performing gene set enrichment analysis in Python. *Bioinformatics* **39**, btac757 (2023).

MAIN FIGURES

Jones*, Sun* *et al.* **Figure 1**

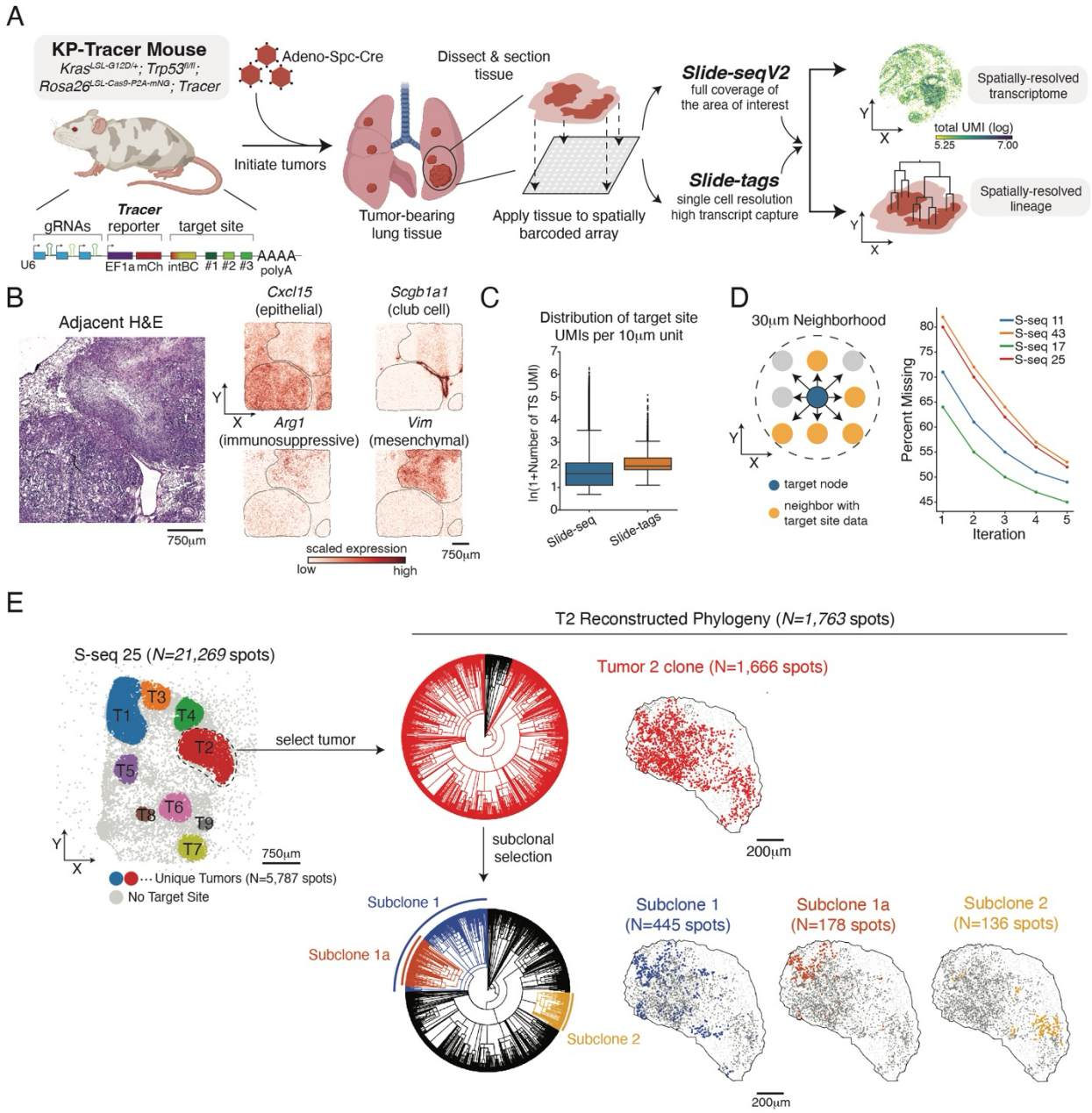

Figure 1. An integrated lineage and spatial platform enables high-resolution analysis of tumor evolution *in vivo*.

(A) Schematic of experimental workflow for integrated, spatially resolved lineage and cell state analysis. In KP-tracer mice, oncogenic *Kras*$^{G12D/+}$;*Trp53*$^{-/-}$ mutations and Cas9-based lineage tracing were simultaneously activated upon administration of adenovirus carrying SPC promoter-driven Cre recombinase. After 12-16 weeks, mice were sacrificed, and cryopreserved tumor-bearing lungs were sectioned for spatial profiling with Slide-seq and Slide-tags technologies. Libraries were prepared and sequenced to study spatially resolved lineages and transcriptional patterns. S-seq 30 is used as a representative example for total UMI capture in a spatial array. Biorender was used to create parts of this schematic.

(B) Representative H&E staining and spatially resolved gene expression data for a lung section carrying three tumors (black line). Log-normalized, scaled counts for epithelial-like (*Cxcl15* and *Scgb1a1*), immunosuppressive myeloid (*Arg1*), and mesenchymal cells (*Vim*) are shown.

(C) Distribution of the number of target-site UMIs for Slide-seq and Slide-tags data. Ln(1+x) counts are shown.

(D) Schematic of spatial imputation of lineage-tracing data in 30μm neighborhoods (left) and representative examples of missingness left after each of 5 iterations of spatial imputation.

(E) Representative spatially resolved lineages in spatial array S-seq 25 profiling a lung section carrying 9 distinct tumors. Reconstructed lineages are displayed for a representative tumor, T2. Successive nested subclones displaying both shared and distinct lineage states in unique colors are indicated on the phylogenetic tree and mapped spatially. Lineages marked in black spots not included in the designated subclone. Overall, spots that are more related in lineage tend to be spatially coherent.

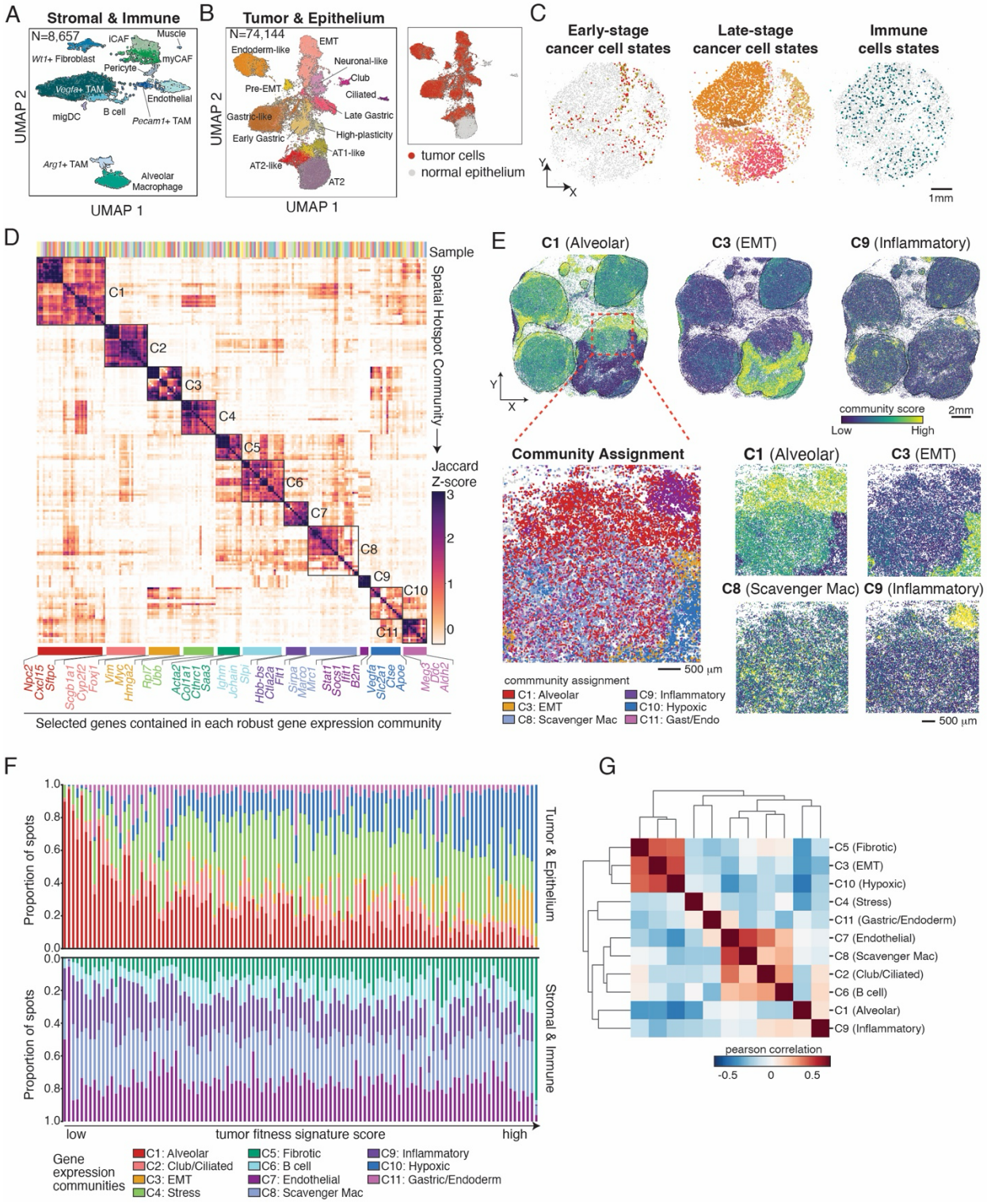
A
Stromal & Immune
N=8,657
ICAF
Muscle
Wt1+ Fibroblast
myCAF
Pericyte
Vegfa+ TAM
Endothelial
B cell
migDC
Pecam1+ TAM
Arg1+ TAM
Alveolar Macrophage
UMAP 2
UMAP 1
B
Tumor & Epithelium
N=74,144
Endoderm-like
EMT
Neuronal-like
Club
Pre-EMT
Ciliated
Gastric-like
Late Gastric
Early Gastric
High-plasticity
AT1-like
AT2-like
AT2
tumor cells
normal epithelium
C
Early-stage cancer cell states
Late-stage cancer cell states
Immune cells states
1mm
D
Sample
Spatial Hotspot Community
Jaccard Z-score
C1
C2
C3
C4
C5
C6
C7
C8
C9
C10
C11
Selected genes contained in each robust gene expression community
E
C1 (Alveolar)
C3 (EMT)
C9 (Inflammatory)
community score
Low
High
2mm
Community Assignment
C1 (Alveolar)
C3 (EMT)
C8 (Scavenger Mac)
C9 (Inflammatory)
500 µm
commmunity assignment
C1: Alveolar
C3: EMT
C8: Scavenger Mac
C9: Inflammatory
C10: Hypoxic
C11: Gast/Endo
F
Proportion of spots
Tumor & Epithelium
Stromal & Immune
low
tumor fitness signature score
high
Gene expression communities
C1: Alveolar
C2: Club/Ciliated
C3: EMT
C4: Stress
C5: Fibrotic
C6: B cell
C7: Endothelial
C8: Scavenger Mac
C9: Inflammatory
C10: Hypoxic
C11: Gastric/Endoderm
G
C5 (Fibrotic)
C3 (EMT)
C10 (Hypoxic)
C4 (Stress)
C11 (Gastric/Endoderm)
C7 (Endothelial)
C8 (Scavenger Mac)
C2 (Club/Ciliated)
C6 (B cell)
C1 (Alveolar)
C9 (Inflammatory)
pearson correlation
-0.5
0
0.5

Figure 2. Diverse spatial gene expression communities emerge during KP-tracer tumor progression.

(A-B) UMAP projections of Slide-tags data on tumor bearing lungs from KP-Tracer mice, annotated by cell type. (A) Slide-tags data corresponding to all stromal and immune cell types: *Cd45*+ immune cells and other non-epithelial stromal cells. (B) Slide-tags data corresponding to all cancer and normal epithelial cells. Inset indicates where cancer cells are found in this projection.

(C) Representative spatial projections of early-stage and late-stage cancer cell states, and immune cell types from Slide-tags analysis of KP-Tracer tumor bearing lung (shown on S-tags 3). Colors correspond to those in UMAP projections in (A-B).

(D) Heatmap of Z-scored Jaccard overlap between genes contained in spatial gene expression communities. Each row or column is a community, defined as a set of spatially autocorrelated genes identified with Hotspot, and robust spatial gene expression communities are determined by hierarchical clustering and indicated by annotated blocks. The Slide-seq sample from which a community is identified is indicated by unique colors on the top of the heatmap. Representative genes specific to each spatial community are highlighted at the bottom of the heatmap.

(E) Community scores of selected spatial communities projected onto a representative Slide-seq dataset of a tumor bearing lung with 4 major tumors (S-seq 43). Tumor boundaries are indicated with black lines (top). Zoom in of region showing community assignments and scores for a selection of communities (bottom).

(F) Proportion of gene expression community assignments across all KP lung tumors in the Slide-seq dataset, ordered by increasing fitness signature scores. Each bar indicates a single segmented tumor in the Slide-seq dataset. Top: communities that are more related to tumor or epithelial programs. Bottom: communities that are related to stromal and immune programs.

(G) Heatmap reporting Pearson correlation of community abundances across all tumors in the Slide-seq data.

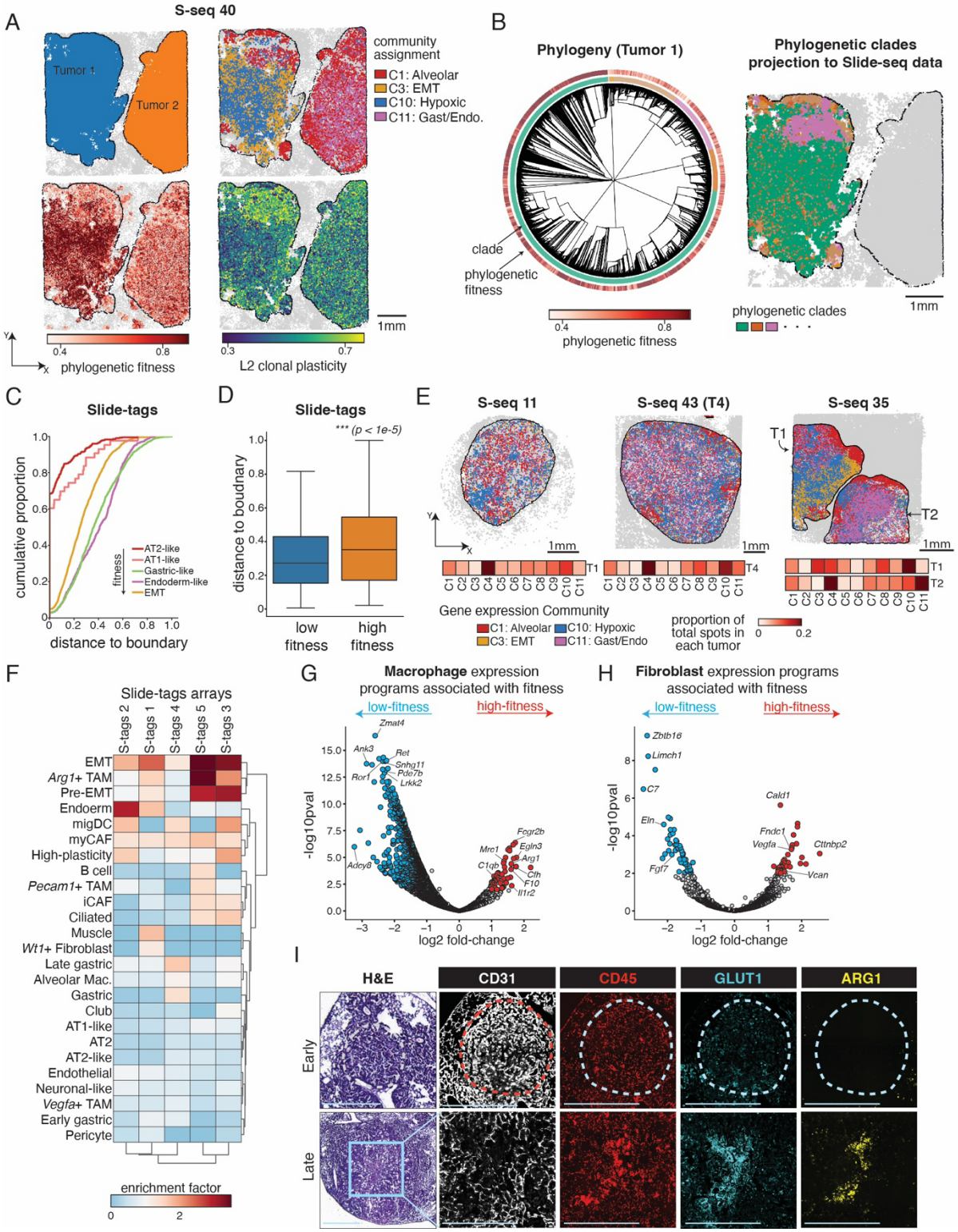
A
S-seq 40
Tumor 1
Tumor 2
community assignment
C1: Alveolar
C3: EMT
C10: Hypoxic
C11: Gast/Endo.
1mm
phylogenetic fitness
L2 clonal plasticity
B
Phylogeny (Tumor 1)
Phylogenetic clades projection to Slide-seq data
clade
phylogenetic fitness
phylogenetic clades
C
Slide-tags
cumulative proportion
distance to boundary
AT2-like
AT1-like
Gastric-like
Endoderm-like
EMT
fitness
D
Slide-tags
*** (p < 1e-5)
distance to boudnary
low fitness
high fitness
E
S-seq 11
S-seq 43 (T4)
S-seq 35
T1
T2
T4
Gene expression Community
C1: Alveolar
C3: EMT
C10: Hypoxic
C11: Gast/Endo
proportion of total spots in each tumor
F
Slide-tags arrays
S-tags 2
S-tags 1
S-tags 4
S-tags 5
S-tags 3
EMT
Arg1+ TAM
Pre-EMT
Endoerm
migDC
myCAF
High-plasticity
B cell
Pecam1+ TAM
iCAF
Ciliated
Muscle
Wt1+ Fibroblast
Late gastric
Alveolar Mac.
Gastric
Club
AT1-like
AT2
AT2-like
Endothelial
Neuronal-like
Vegfa+ TAM
Early gastric
Pericyte
enrichment factor
G
Macrophage expression programs associated with fitness
low-fitness
high-fitness
-log10pval
log2 fold-change
Zmat4
Ank3
Ret
Snhg11
Pde7b
Ror1
Lrkk2
Adcy8
Fcgr2b
Egln3
Mrc1
Arg1
C1qb
Cth
F10
Il1r2
H
Fibroblast expression programs associated with fitness
low-fitness
high-fitness
-log10pval
log2 fold-change
Zbtb16
Limch1
C7
Eln
Fgf7
Cald1
Fndc1
Vegfa
Cttnbp2
Vcan
I
H&E
CD31
CD45
GLUT1
ARG1
Early
Late

Figure 3. Subclonal expansions associate with microenvironmental remodeling towards a hypoxic, fibrotic, and immunosuppressive state.

(A) A representative Slide-seq array containing two tumors (S-seq 40) is shown with spatial projections of tumor annotations, selected gene expression community assignments, phylogenetic fitness, and L2 clonal plasticity.

(B) Reconstructed phylogeny and spatial localization of phylogenetic subclades for Tumor 1 from the representative Slide-seq dataset (S-seq 40) example shown in (A). The phylogeny is annotated by subclonal clade assignment (inner color track) and phylogenetic fitness (outer color track).

(C) Cumulative density distributions for normalized Euclidean distance to nearest non-tumor cell (i.e., tumor boundary) for five selected major cancer cell states across all Slide-tags arrays. Cancer cells in high-fitness-associated cell states (e.g. EMT, Endoderm-like, Gastric-like) locate further away from the tumor boundary than those in low-fitness-associated states (AT2-like, AT1-like). Distance is normalized to unit scale (0-1).

(D) Distribution of normalized Euclidean distances to nearest non-tumor cell (i.e., tumor boundary) for high-fitness and low-fitness cells (defined here as having phylogenetic fitness greater than the 90th or less than the 10th percentiles, respectively). High-fitness cells are significantly further away from the tumor boundary ($p<1e-5$, wilcoxon rank-sums test).

(E) Representative Slide-seq examples showing the evolution of the spatial gene expression communities following tumor progression (left to right). Selected community assignments are displayed, and full proportion of assignments are reported in 1D heatmaps under each spatial dataset.

(F) Clustered heatmap of enrichments of cell type abundances in spatial neighborhoods of high- and low-fitness cells in 5 Slide-tags arrays. Values > 1 indicate that a cell type is more abundant (i.e., enriched) in neighborhoods of cells with high fitness. Cell type names are identical to those reported in **Figure 2A-B**.

(G-H) Differential expression analysis of (G) macrophage and (H) fibroblast polarization states in neighborhoods of high- and low-fitness cells from Slide-tags arrays. Each dot is a gene, and significant hits (log2|FC| >= 1 and false-discovery-rate adjusted p-value < 0.05) are reported in red and blue. Red genes are up-regulated in neighborhoods of high-fitness cells, and blue genes are down-regulated. Significant GO terms are reported in **Supplementary Table 1**.

(I) H&E and paired immunofluorescence staining of endothelial-cell marker CD31, immune cell marker CD45, hypoxia-reporter GLUT1, and immunosuppressive myeloid marker ARG1

in representative KP tumors. The interior of large, late-stage tumors is marked with a decrease of endothelial cells (CD31) and increases of hypoxia (GLUT1) and immunosuppressive myeloid cells (ARG1, CD45). Scale bars = 1mm.

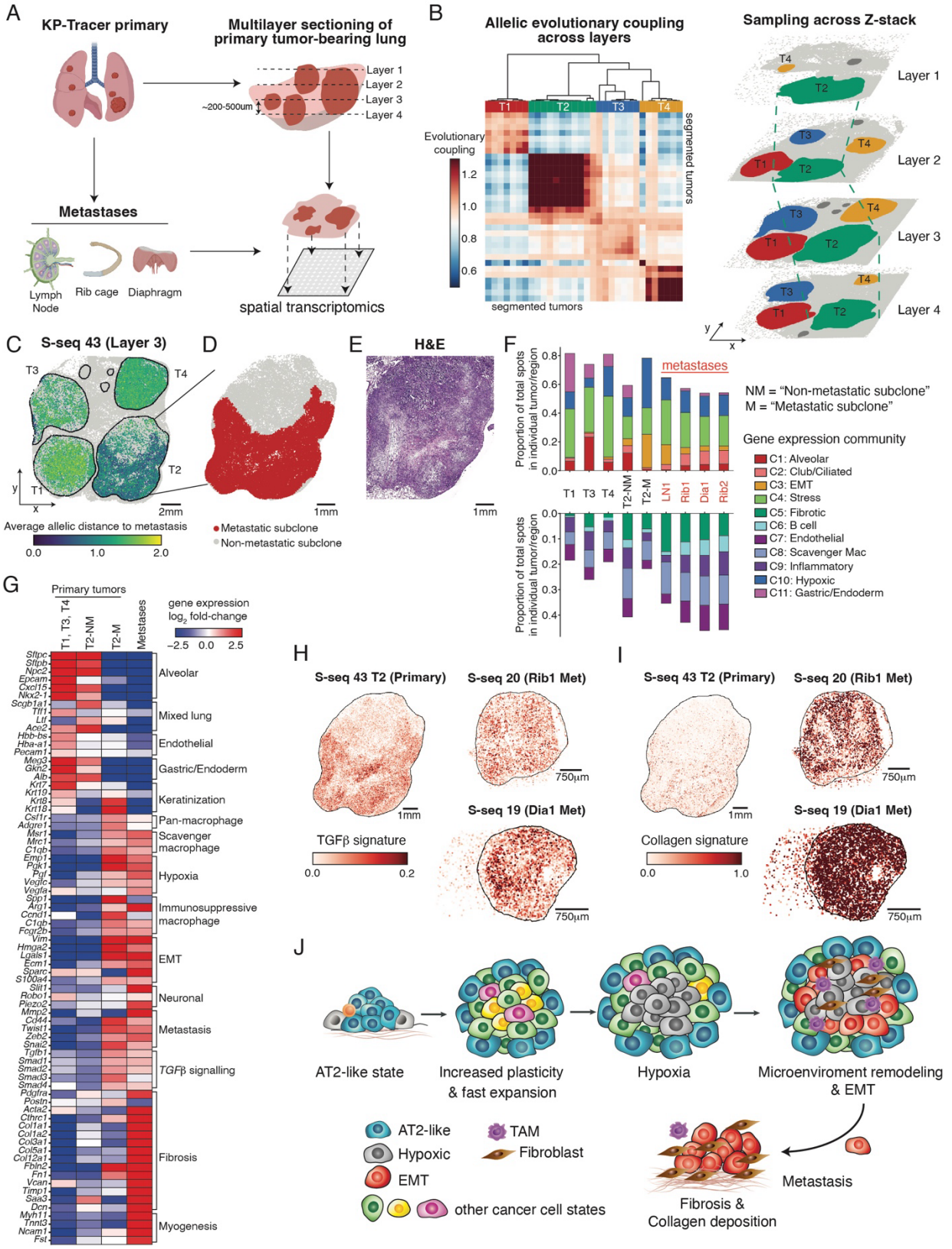
A
KP-Tracer primary
Multilayer sectioning of primary tumor-bearing lung
Layer 1
Layer 2
Layer 3
Layer 4
~200-500um
Metastases
Lymph Node
Rib cage
Diaphragm
spatial transcriptomics
B
Allelic evolutionary coupling across layers
Evolutionary coupling
segmented tumors
Sampling across Z-stack
C
S-seq 43 (Layer 3)
Average allelic distance to metastasis
D
Metastatic subclone
Non-metastatic subclone
E
H&E
F
metastases
NM = "Non-metastatic subclone"
M = "Metastatic subclone"
Gene expression community
C1: Alveolar
C2: Club/Ciliated
C3: EMT
C4: Stress
C5: Fibrotic
C6: B cell
C7: Endothelial
C8: Scavenger Mac
C9: Inflammatory
C10: Hypoxic
C11: Gastric/Endoderm
Proportion of total spots in individual tumor/region
G
Primary tumors
gene expression log2 fold-change
Alveolar
Mixed lung
Endothelial
Gastric/Endoderm
Keratinization
Pan-macrophage
Scavenger macrophage
Hypoxia
Immunosuppressive macrophage
EMT
Neuronal
Metastasis
TGFβ signalling
Fibrosis
Myogenesis
H
S-seq 43 T2 (Primary)
S-seq 20 (Rib1 Met)
S-seq 19 (Dia1 Met)
TGFβ signature
I
Collagen signature
J
AT2-like state
Increased plasticity & fast expansion
Hypoxia
Microenviroment remodeling & EMT
AT2-like
Hypoxic
EMT
TAM
Fibroblast
other cancer cell states
Fibrosis & Collagen deposition
Metastasis

Figure 4. Tracing the evolution of subclonal niches across the metastatic cascade.

(A) Schematic of spatial transcriptomics workflow from a KP-Tracer mouse with large primary lung tumors and paired metastases from the lymph node, rib cage, and diaphragm. Multiple lung sections with four large primary tumors were harvested and subjected to both Slide-seq and Slide-tags assays. Biorender was used to create parts of this schematic.

(B) Coarse-grained alignment of Slide-seq spatial transcriptomics data (based on lineage-tracing edits) from four representative layers (Layer 1 – Layer 4) of a KP tumor bearing lung at approximately 200-500μm intervals from different z position. (Left) A clustered heatmap of allelic evolutionary coupling scores across all Slide-seq datasets from the tumor-bearing lung identifies the four major tumors. Each row or column is a single tumor from one Slide-seq dataset. (Right) 3D reconstruction of aligned datasets, annotated by one of four major tumors. Individual tumors are labeled in different colors.

(C) Representative spatial projection (S-seq 43) of allelic distances – summarizing how different lineage-tracing edits are between cells – for each spot with lineage-tracing data. Distance was computed to a consensus metastatic parental allele and normalized between 0 and 2.

(D-E) The metastasis-initiating subclone in T2 was segmented from cells with high relatedness to metastatic tumors and labeled in red. (E) H&E staining of T2.

(F) Proportion of gene expression community across representative stages of the metastatic cascade, including primary lung tumors (T1,3,4) without relatedness to metastases, the metastasis-initiating (M) and non-metastatic-initiating (NM) subclones in the primary tumor (T2) that gave rise to metastases, and four metastases. Top: communities that are more related to tumor or epithelial programs. Bottom: communities that are related to stromal/immune programs.

(G) Heatmap of gene expression log2-fold-changes between environmental niche (primary tumors without metastatic relationship, non-metastasis-initiating (NM) and metastasis-initiating (M) subclones within T2, and metastases). Genes are manually organized into ontologies.

(H-I) Spatial projection of gene expression scores of the Hallmark TGFβ and Collagen gene signatures on the metastasis-initiating primary tumor and selected metastases. Tumor 2 on S-seq 43 is used as the representative layer.

(J) A schematic model of KP tumor evolution and microenvironmental remodeling.

SUPPLEMENTARY FIGURES

Jones*, Sun* et al. **Supplemental Figure 1**

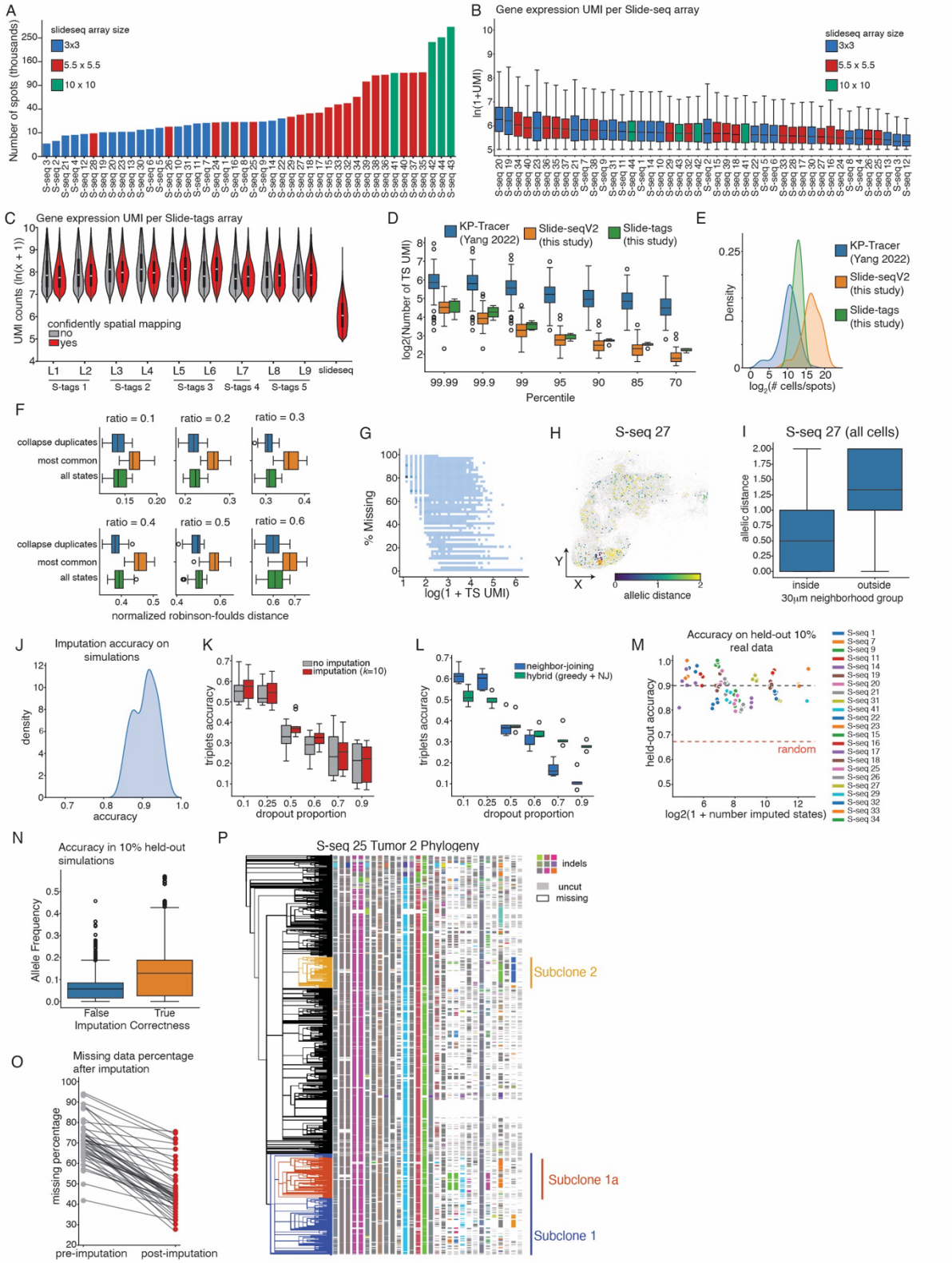

Figure S1. Characterization of spatial-lineage platform and benchmarking of computational approaches. Related to Figure 1.

(A) Number of spots that pass quality-control for all Slide-seq array. 3mm, 5mm, and 1cm arrays are uniquely colored.

(B) Number of gene expression UMIs for each Slide-seq array. Ln(1+UMI) is reported for each dataset. 3mm, 5mm, and 1cm arrays are uniquely colored.

(C) Number of gene expression UMIs for each Slide-tags array, and one representative Slide-seq array. Each array is sequenced across multiple 10X libraries; assignment of 10X library to array is annotated. Distributions are split between cells that are confidently mapped and those that are not. Ln(1+UMI) is reported.

(D) Distribution of number of target-site UMIs marking the top *X* percentile for whole-cell (KP-Tracer), Slide-seq, or Slide-tags datasets. Ln(1+UMI) is reported.

(E) Distribution of number of observations (cells or spots) that pass target-site quality-control in whole-cell (KP-Tracer), Slide-seq, or Slide-tags datasets. Log_2 of the number of observations is reported.

(F) Normalized Robinson-Foulds reconstruction error for simulated trees with increasing ratios of pooled cells and different pre-processing techniques. A ratio of *p* indicates that simulated lineage-tracing data of *p*% of cells are combined into a single observation to simulate multiple-cell capture in spatial transcriptomics (**Methods**).

(G) Relationship between percentage of missing lineage-tracing data in a cell or spot and the log-number of UMIs (ln(1+x)) for Slide-seq and Slide-tags data.

(H) Representative example of spatial coherence of lineage-tracing data on S-seq 27. For a selected spot (shown as a star), normalized allelic distance is reported for all spots with confident lineage-tracing data. Allelic distance is normalized between 0 and 2.

(I) Distribution of allelic distances to spots within a $30\mu m$ neighborhood of a spot versus outside this neighborhood. Distribution over all spots in S-seq 27 is reported.

(J) Distribution of spatial imputation accuracy in lineage-tracing data simulated on a two-dimensional array.

(K) Triplets-correct accuracy of reconstructed phylogenies simulated on a spatial array for various amounts of missing data rates, with and without spatial imputation.

(L) Triplets-correct accuracy of reconstructions with modified Neighbor-Joining and hybrid Cassiopeia-Greedy / Neighbor Joining algorithms for data simulated on a spatial array with various amounts of missing data, after spatial imputation.

(M) Accuracy of spatial imputation and number of imputed states after holding-out 10% of all lineage-tracing data in Slide-seq datasets. Datasets where at least 10 imputations are made are shown. Median accuracy of random predictions is reported in a red dashed line.

(N) Allele frequency of held-out data in a given tumor binned by imputation correctness.

(O) Overview of missing data reduction across all Slide-seq datasets after five rounds of spatial-imputation.

(P) Phylogeny and lineage tracing heatmap of tree reconstructed in **Figure 1E**. Subclones of interest are annotated in the same colors as in **Figure 1E**. Unique colors of the heatmap indicate unique insertions or deletions ("indels"), white indicates missing data, and gray colors indicates no indel detected.

Jones*, Sun* *et al.* **Supplemental Figure 2**

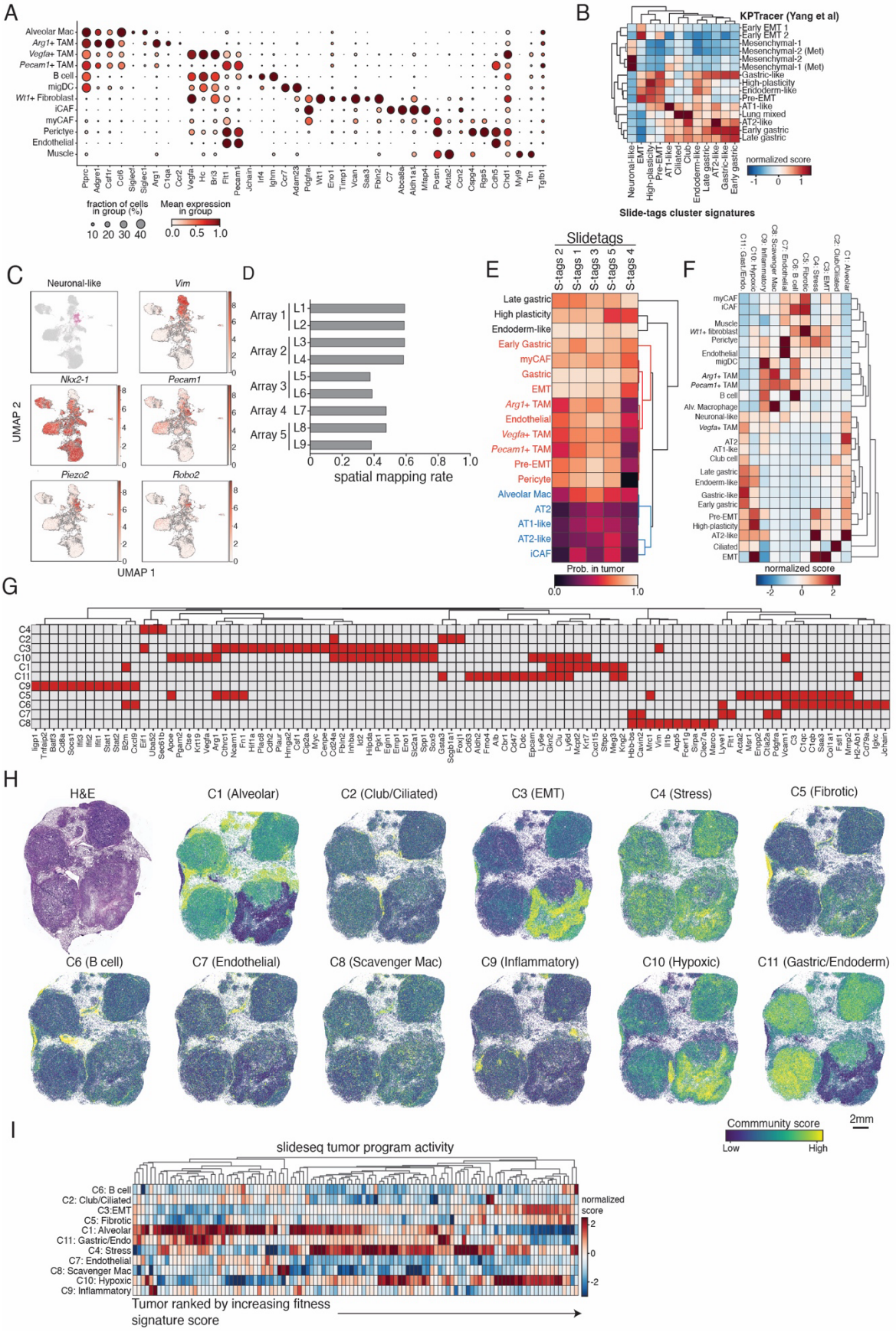

Figure S2. Profiling of cell types and spatial communities underlying tumor progression. Related to Figure 2.

(A) Summary of gene markers for each stromal cell population identified in Slide-tags. Each row corresponds to a stromal or immune cell-type cluster and each column corresponds to a marker gene. Dot size indicates the proportion of cells expression that gene, and color indicates the average gene expression value (unit scaled between 0 and 1).

(B) Clustered heatmap of transcriptional score of marker genes identified from Slide-tags data of tumor and epithelial cell types applied to previous KP-Tracer data. Scores are Z-normalized.

(C) Annotation of Slide-tags tumor and epithelial UMAP projection with the Neuronal-like cell-type, and log-normalized gene expression patterns of selected genes: *Vim*, *Nkx2-1, Pecam1, Piezo2,* and *Robo2.*

(D) Proportion of cells that are confidently mapped in each Slide-tags array.

(E) Proportion of cells for each cell type that are found within the tumor boundary across Slide-tags arrays.

(F) Clustered heatmap of transcriptional scores for each spatial community, identified from Hotspot analysis of Slide-seq data, for each Slide-tags cell type cluster. Scores are Z-normalized.

(G) Clustered heatmap showing selected genes for each spatial community. Red colors indicate that a gene is found within that module.

(H) Community scores for each spatial community and paired H&E for a representative Slide-seq community.

(I) Clustered heatmap of community scores for each tumor in the Slide-seq dataset ordered by increasing fitness signature scores. Scores are Z-normalized.

Jones*, Sun* *et al.* **Supplemental Figure 3**

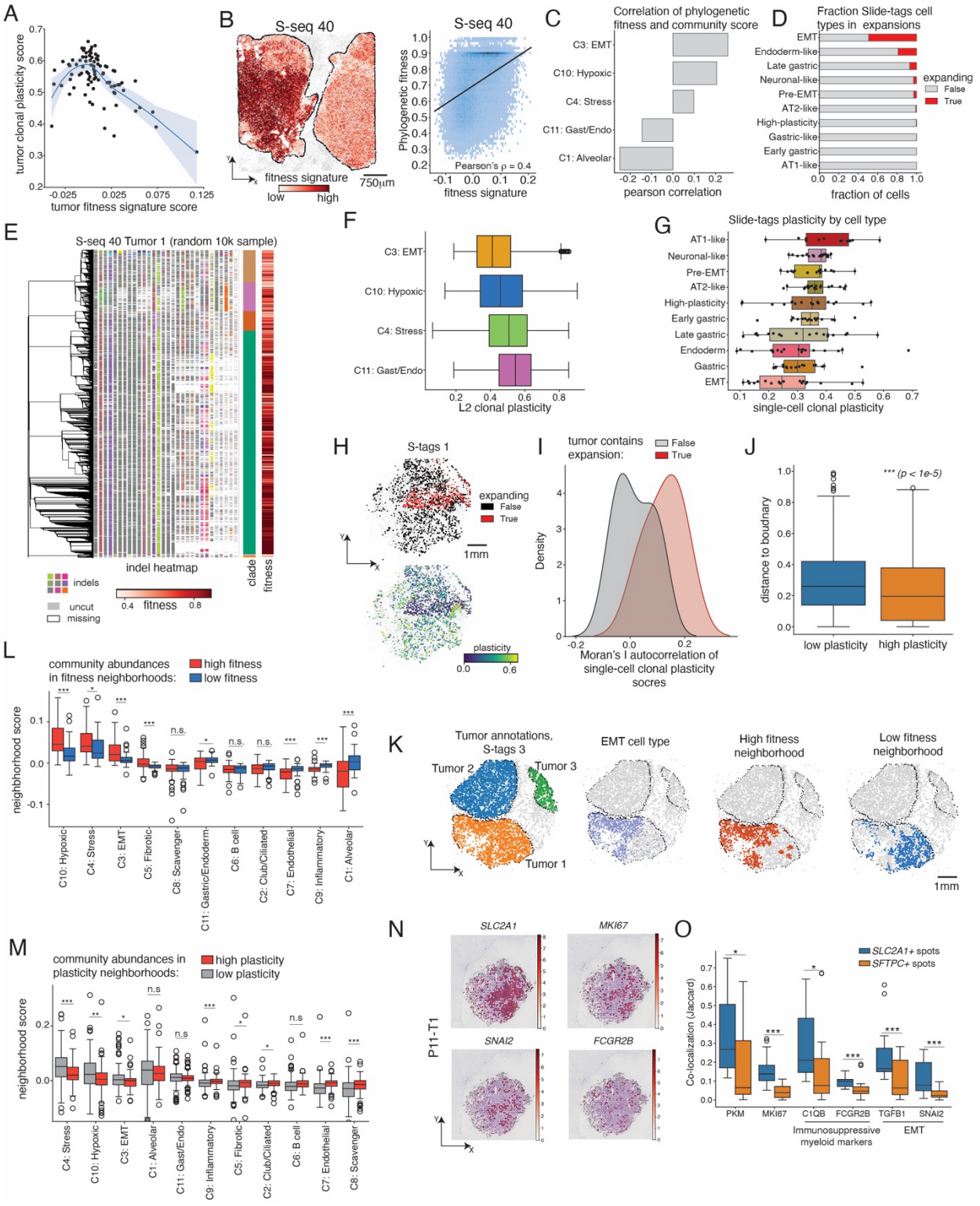

Figure S3. Characterization of subclonal tumor and microenvironmental dynamics. Related to Figure 3.

(A) Joint distribution of mean tumor clonal plasticity and fitness signatures across Slide-seq datasets.

(B) Relationship between phylogenetic fitness, estimated from inferred trees, and transcriptional fitness signature score (Pearson's correlation = 0.4)

(C) Correlation of phylogenetic fitness, estimated from inferred trees, and community scores for cancer-associated communities (C1: Alveolar; C3: EMT; C4: Stress; C10: Hypoxic; and C11: Gastric/Endoderm). Correlations are ordered in decreasing order.

(D) Fraction of cells found in expanding regions of Slide-tags phylogenies, summarized for each cancer cell-type.

(E) Reconstructed phylogeny and lineage tracing heatmap of representative tumor presented in **Figure 3A-B**. Unique colors of the heatmap indicate unique insertions or deletions ("indels"), white indicates missing data, and gray colors indicates no indel detected. Color bars indicate the subclonal clade and fitness, identical to those reported in **Figure 3A-B**.

(F) Distribution of L2 clonal plasticity (**Methods**) quantified in Slide-seq phylogenies summarized across spots annotated by cancer-dominated communities.

(G) Distribution of single-cell clonal plasticity scores computed in Slide-tags phylogenies, stratified by cancer cell-types, and reported across tumor-array combinations.

(H) Representative spatial localization of phylogenetic expansion (top) and single-cell clonal plasticity scores (bottom) in a single Slide-tags array (S-tags 3). Scale bar indicates 1mm.

(I) Distribution of autocorrelation values, computed by Moran's I, of single-cell clonal plasticity scores for tumors with or without expansions. Higher autocorrelation values indicate that values have higher spatial coherence. Autocorrelations are reported across all Slide-tags datasets.

(J) Distance to nearest non-tumor cell (i.e., tumor boundary) for high- and low-plasticity cells across all Slide-tags arrays. Cells with high-plasticity are closer to the tumor boundary ($p < 1e\text{-}5$, wilcoxon rank-sums test).

(K) Representative example demonstrating the stratification of neighborhoods of high- and low-fitness cells in Slide-tags data, and comparison to spatial localization of the EMT state. Scale bar indicates 1mm.

(L) Distribution of average community scores in $30\mu m$ neighborhoods of high- or low-fitness spots in Slide-seq data. Each observation corresponds to a tumor. Significance is

indicated above each comparison (*n.s.* = not significant; * = *p<0.1*; ** = *p<0.05;* *** = *p < 0.01*).

(M) Distribution of average community scores in 30μm neighborhoods of high- or low-plasticity spots in Slide-seq data. Each observation corresponds to a tumor. Significance is indicated above each comparison (*n.s.* = not significant; * = *p<0.1*; ** = *p<0.05;* *** = *p < 0.01*).

(N) Representative example of spatial log-normalized gene expression values for selected genes in a human lung adenocarcinoma (LUAD) spatial transcriptomics dataset (see **Methods**).

(O) Overall distribution of log-normalized gene expression values of selected genes co-expressed in hypoxic (*SLC2A1*+) or epithelial-like (*SFTPC*+) tumor spots across all LUAD samples in dataset shown in (M). Ontologies are indicated underneath genes. Hypoxia+ spots have higher expression of proliferation (*MKI67)*, immunosuppressive myeloid (*FCGR2B* and *C1QB)* and EMT (*SNAI2* and *TGFB1*) markers. Statistical significance between gene expression distributions is shown for each comparison (*n.s.* = not significant; * = *p<0.1*; ** = *p<0.05;* *** = *p < 0.01*).

Jones*, Sun* *et al.* **Supplemental Figure 4**

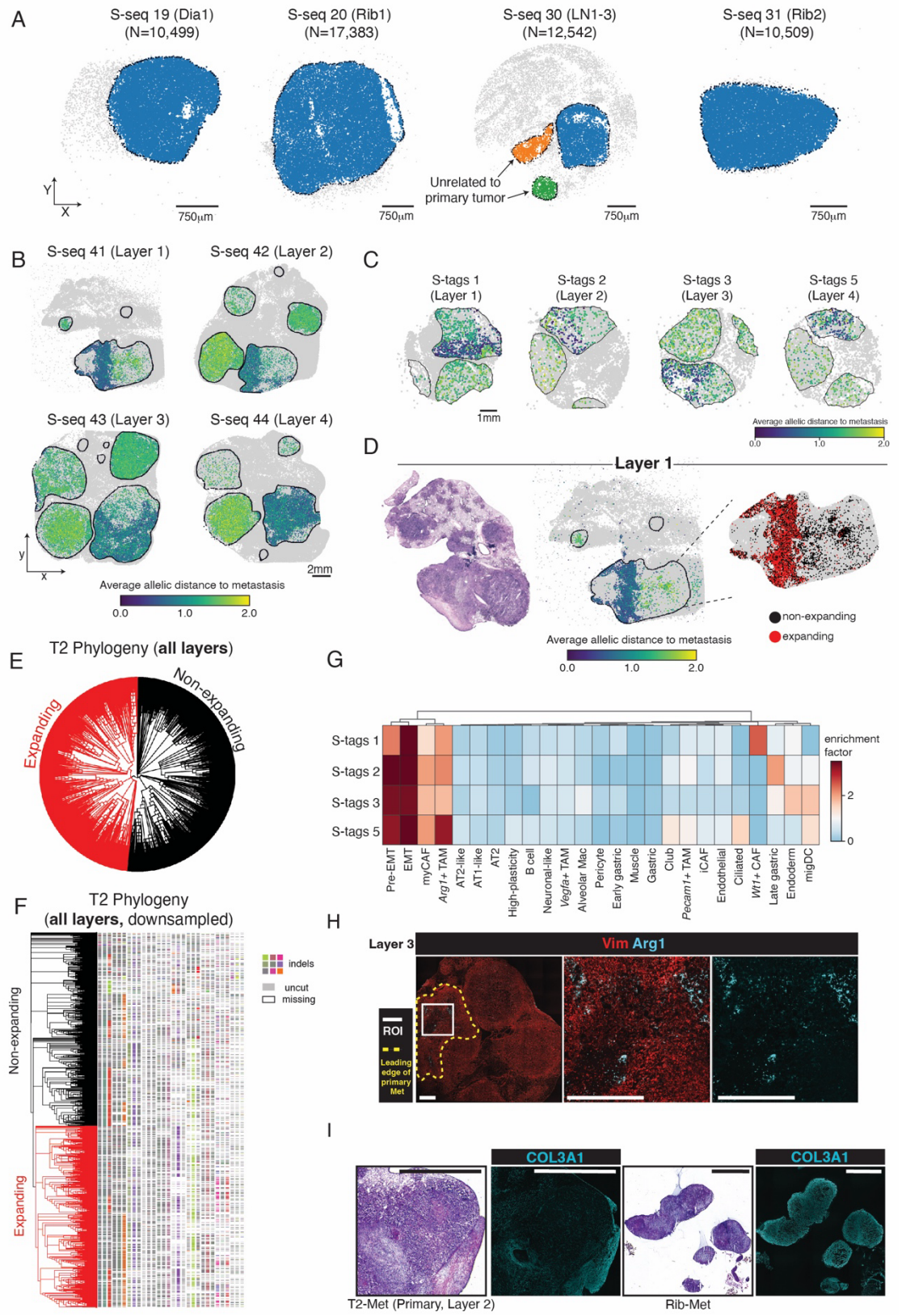

Figure S4. Profiling of metastases and microenvironmental evolution during metastasis. Related to Figure 4.

(A) Summary of metastases identified in Slide-seq spatial transcriptomics dataset. Each sample is annotated the metastatic site (LN: lymph node; Dia: Diaphragm). Two metastases in the lymph node (S-seq 30) were not found to be related to the primary tumor studies in **Figure 4** and thus removed from comparative analysis.

(B) Spatial projection of allelic distances for each spot with lineage-tracing data to consensus metastatic parental allele across all four layers profiled in Slide-seq. Allelic distances are normalized between 0 and 2.

(C) Spatial projection of allelic distances for each cell with lineage-tracing data to consensus metastatic parental allele across paired Slide-tags arrays. Allelic distances are normalized between 0 and 2.

(D) H&E staining, spatial mapping of allelic distances to consensus metastatic parental allele state, and spatial localization of phylogenetic expansion for T2 in representative dataset. Allelic distances are normalized between 0 and 2.

(E) Reconstructed phylogeny of T2 from all layers with phylogenetic expansion annotated in red.

(F) Reconstructed phylogeny and lineage tracing heatmap of T2 from all layers. Unique colors of the heatmap indicate unique insertions or deletions ("indels"), white indicates missing data, and gray colors indicates no indel detected. Clades participating in expansion shown in (E) are shown in red.

(G) Clustered heatmap of enrichments of cell type abundances in spatial neighborhoods of cells related to metastases in Slide-tags arrays.

(H) Immunofluorescence imaging of ARG1 and VIM in a section of the tumor-bearing lung close to Layer 3. Leading edge of the metastasis-initiating subclone is indicated with yellow dashed line. Scale bar indicates 1mm.

(I) H&E and immunofluorescence imaging of COL3A1 in a section of the metastasis-initiating primary tumor (Layer 2) and related metastasis. Scale bar indicates 1mm.